Quantification of Phase Transformation in Stainless Steel 301LN Sheets

By

Allison M. Beese
B.S. Mechanical Engineering
Pennsylvania State University, 2005

SUBMITTED TO THE DEPARTMENT OF MECHANICAL ENGINEERING IN PARTIAL FULFILLMENT OF THE REQUIREMENTS FOR THE DEGREE OF

MASTER OF SCIENCE IN MECHANICAL ENGINEERING
AT THE
MASSACHUSETTS INSTITUTE OF TECHNOLOGY

JUNE 2008

Signature of Author: _____
Department of Mechanical Engineering
April 28, 2008

Certified by: _____
Tomasz Wierzbicki
Professor of Applied Mechanics
Thesis Supervisor

Accepted by: _____
Lallit Anand
Professor of Mechanical Engineering
Chairman, Committee for Graduate Students

Quantification of Phase Transformation in Stainless Steel 301LN Sheets

by

Allison M. Beese
Submitted to the Department of Mechanical Engineering
on April 28, 2008 in partial fulfillment of the
requirements for the Degree of Master of Science in
Mechanical Engineering

ABSTRACT

This thesis investigates the large deformation behavior of stainless steel 301LN cold-rolled sheets which is largely governed by the initial anisotropy combined with the phase transformation during deformation. Stainless steel offers high strength with relatively high ductility as compared with other structural steels. The effect of initial anisotropy on the strength in different material directions is studied in order to predict forming and crash response of vehicle components. It is observed that loading in the material rolling direction results in increased strength in the cross direction, however loading in the material cross-rolling direction results in decreased strength in the rolling direction. The mechanism responsible for the above cross-hardening is complex and requires investigation of the microstructural evolution of the sheets.

The austenitic stainless steel studied is comprised of only austenite when in bulk form. However, the process of cold-rolling the bulk material into sheets results in strain-induced martensitic phase transformation. Additional straining of the material leads to even more transformation of austenite to martensite. Because martensite is a harder phase than austenite, micromechanical arguments suggest that the amount of martensite has an effect on the plasticity and eventual fracture of this material.

In this thesis, the martensitic evolution as a function of material direction and strain level is measured using three different techniques: X-ray diffraction, microscopy, and magnetic induction. The first two methods require interrupted tests, while using a Feritscope allows for in-situ measurement of the martensite content. However, the Feritscope must be calibrated by another measurement method. Observations of the measurements from each of the three methods confirm that the output of the Feritscope, Ferrite Number, is proportional to the martensite content. Therefore in-situ tests employing the Feritscope will allow for monitoring of the martensite content with evolution of stress and strain. From experiments described here, a directional dependence on martensite content is observed. The results from this study can be used to formulate an anisotropic martensite transformation kinetics law to describe the evolution of martensite content as a function of material anisotropy, stress state, and strain state.

Thesis Supervisor: Tomasz Wierzbicki
Title: Professor of Applied Mechanics

TABLE OF CONTENTS

TABLE OF FIGURES

TABLE OF TABLES

ACKNOWLEDGMENTS

First, I would like to offer my sincere thanks to my advisor, Professor Tomasz Wierzbicki, for his guidance and support throughout my first two years at MIT - for presenting me with challenges and offering me the encouragement and resources to meet them. Additionally, I am very grateful to Professor Wierzbicki for funding my first year at MIT through a Research Assistantship in the Impact and Crashworthiness Lab. I would also like to express my gratitude to Professor Dirk Mohr for his mentorship, his patience, and his valuable insight into my research.

Many thanks are due Professor David Parks for his enthusiasm for my research and for several instructive discussions on strain-induced phase transformation.

In addition, I thank Dr. Pierre-Olivier Santacreu and Dr. Benoit Proult of Arcelor-Mittal for their consultations on micrography and metallurgy.

I am indebted to: Dr. Scott Speakman who helped me conduct the X-ray diffraction studies and subsequent analysis; Dr. Yinlin Xie for allowing me to use her polishing lab; Pierce Hayward for his help with the electronics of my experimental setup; and Harold Larson for his help with metallurgy.

I would like to thank all the members of the ICL for creating a cooperative working environment in which we all support and help each other. Thanks to: Dr. Yuanli Bai, Dr. Yaning Li, Mr. Carey Walters, Mr. JongMin Shim, Mr. Meng Luo, and Ms. Danielle Issa, as well as Sheila McNary.

I am very grateful to the Department of Defense for awarding me a National Defense Science and Engineering Graduate fellowship to fund three years of my study and research at MIT.

Finally, my deepest gratitude goes to my family and to Michael for their unconditional love, support and encouragement.

Chapter 1: Introduction

In metallic materials, a tradeoff typically exists between ductility and strength. However, Advanced High Strength Steels (AHSS) are able to offer very high strength with relatively high ductility. These types of steels prove to be an attractive material from which to make components in automotive and aircraft industries, one reason being that they can eventually lead to weight reduction and therefore reduced fuel consumption in these vehicles. In order to more accurately model components so that failure is predicted and avoided, a constitutive model describing the material plasticity and fracture must be created and subsequently implemented into a finite element code. The steel addressed in this study is austenitic stainless steel of the European classification 18-7L C1000, which is also classified as AISI stainless steel 301LN. This thesis begins to examine the evolving microstructure to better understand the macroscopic behavior of stainless steel 301LN.

In stainless steel 301LN, the bulk material is entirely composed of austenite. After the steel is cold-rolled into sheets, some of the austenite transforms to martensite, which is a stronger, more brittle phase. In addition, this cold-rolling introduces anisotropy in the material. During additional deformation, more of the austenite is transformed to martensite by strain-induced phase transformation. Because martensite is harder and more brittle, it is hypothesized that the martensite content will affect the fracture as well as the plasticity of the metal. In order to understand the initial anisotropy in the material, as well as the differential hardening behavior in different material directions, the microstructural phase transformation is studied.

A series of experiments are performed to examine the evolution of the martensite content in the material. The martensite content is measured using multiple methods. The first method requires interrupted tests and employs X-ray diffraction to determine the relative amounts of the austenitic and martensitic phases. The second method, also requiring interrupted tests, involves creating micrographs of the strained specimens to determine the area percentage in a polished plane, as well as the spatial distribution of martensite. The third method allows for in-situ measurements of martensite volume

percentage using a Feritscope, which employs a magnetic induction method to measure the magnetic martensite content.

The ultimate goal of this research is to develop an anisotropic martensite transformation kinetics law to describe the evolution of martensite content as a function of material anisotropy, stress state, and strain state. This transformation law will then be incorporated into the anisotropic plasticity model detailed in Mohr and Jacquemin 2008, which requires a martensitic evolution law to formulate a non-associated anisotropic hardening model for the same stainless steel 301LN sheets. The transformation law will then be integrated into the ABAQUS user subroutine that implements this plasticity model. Validation tests will be performed in different material directions subjected to various stress states.

1.1 Research on Anisotropic Yield Criteria

There has been extensive research performed on the initial yield surface of many materials. These studies resulted in several proposed yield functions and subsequent plasticity models (e.g., Hill, 1948; Barlat and Lian, 1989; Hill 1990; Barlat 1991; Karafillis and Boyce 1993; and many others). While these models are able to accurately capture the initial yield of several anisotropic materials, they assume isotropic hardening, which predicts the same hardening curve shape for all material directions. There has been recent work on trying to capture anisotropic hardening in order to more accurately simulate the behavior of the material up to fracture (e.g., Plunkett et al., 2006).

A measure typically used to define the degree of anisotropy is the Lankford ratio. This parameter, referred to as "r," is the ratio of strain in the width direction, ε_2, versus strain through the thickness, ε_3, of a specimen subjected to uniaxial tension in the longitudinal direction, with a strain of ε_1, and is given by:

$$r = \frac{\varepsilon_2}{\varepsilon_3} \tag{1}$$

Assuming plastic incompressibility, it follows that

$$\varepsilon_3 = -(\varepsilon_1 + \varepsilon_2), \text{ and therefore } r = \frac{-\varepsilon_2}{(\varepsilon_1 + \varepsilon_2)} \tag{2}$$

This ratio is measured throughout uniaxial tension tests performed for this thesis, and it is found to be reliably constant throughout each of the tests. In the material directions studied in uniaxial tension, the following values are found: $r_0 = 0.6$, $r_{45} = 0.7$, $r_{90} = 0.8$.

1.2 Research on Phase Transformation

Certain austenitic stainless steels may undergo phase transformation from austenitic face-centered-cubic (FCC) crystal structures to martensitic body-centered-cubic (BCC) crystal structures during mechanical loading. Much research on the subject of phase transformation in austenitic stainless steels was performed by Olsen and Cohen, and key findings in their 1975 and 1982 papers are summarized here. The phase transformation in austenitic stainless steels may be either stress-induced or strain-induced. The difference between these two mechanisms can be described by either the region in which the phase transformation occurs (elastic or plastic loading regime) or the nucleation sites of phase transformation. Stress-induced phase transformation occurs when the transformation stress level in the steel is less than the austenite yield stress, leading to phase transformation in the elastic regime (Diani and Parks, 1998). This transformation occurs at nucleation sites that trigger spontaneous transformation on cooling. Strain-induced phase transformation occurs when this transformation stress level is higher than the austenite yield stress, and thus the austenitic phase is plastically deformed, leading to dislocation motion and slip bands in the austenite (Diani and Parks, 1998). These slip bands may be comprised of ε-martensite, which has a hexagonal-close-packed (HCP) crystal structure, mechanical twins, or dense stacking faults. Strain-induced α'-martensite (BCC) forms at the intersections of these slip bands.

Several isotropic models for the strain-induced phase transformation have been developed. Olsen and Cohen (1975) describe a kinematic transformation law that relates the amount of martensite to the amount of plastic strain and the temperature. Subsequent research by Stringfellow et al. (1992) resulted in extension of the Olsen and Cohen 1975 model to incorporate the dependence of phase transformation on stress state. Because martensite has different mechanical properties than austenite, researchers have provided constitutive models that describe the macroscopic flow strength of the austenitic steels depending on the relative compositions of austenite and martensite. Some authors have

chosen to use a rule of mixtures by treating the steel as a composite with the material properties weighted by the relative amounts of austenite and martensite (e.g., Lecroisey and Pineau 1972, Santecreu et al. 1986). Stringfellow et al. (1992) used a more complicated homogenization method to determine the flow strength versus martensite content.

1.3 Material Studied

Austenitic stainless steel sheets of the European specification 18-7L C1000 (AISI stainless steel 301LN) provided by the Joint MIT/Industry AHSS Consortium member Arcelor-Mittal are used for this study. According to the specifications, this type of steel contains 17% chromium, 7% nickel, 0.0025% carbon, and 0.15% nitrogen. The C1000 specification indicates that the 1.5 *mm* thick sheets were fabricated by cold-rolling. The material was shipped in the form of 200 *mm* x 300 *mm* sheets. The mass density of this material is 7.9 g/cm^3. For calculations of plastic strains, the elastic modulus is taken to be 200 *GPa* and the Poisson ratio is taken to be 0.3.

Chapter 2: Uniaxial Behavior of Stainless Steel 301LN Sheets

To begin the investigation of stainless steel 301LN, uniaxial tension tests are performed in three material directions. The gauge width of the specimens is 12.5 *mm*, and the geometry of the specimens follows ASME Standard E8M-04. The purpose of these tests is to determine the extent of anisotropy present in the cold-rolled steel sheets. Uniaxial tension specimens with their tensile axes aligned with either the material rolling direction (denoted 0^{o}), the material cross rolling direction (denoted 90^{o}), or 45 degrees from the material rolling direction (denoted 45^{o}) are strained to fracture to create true stress versus logarithmic strain curves shown in Figure 1. Because of the nonlinearity in the stress-strain curves, the initial yield stress in this study is found by taking the tangent to the stress-strain curve at 2% total strain and extrapolating this line back to the stress value at 0% strain. It is determined that the yield stress in the material rolling direction, s_0, is 876 *MPa*, and the yield stress in the material cross-rolling direction, s_{90}, and 45 degrees from the material rolling direction, s_{45}, is 913 *MPa*. In addition to the directional dependence of initial yield strength, the subsequent hardening curves are quite different.

Based on the true stress versus true strain curves produced under uniaxial tension in the rolling direction, it can be concluded that it is likely that the steel being tested does undergo an austenite to martensite phase transformation. Figure 1 shows a plateau where the stress levels off as the strain increases. This is a typical feature of a stress-strain curve undergoing austenitic-to-martensitic phase transformation. Research has shown that during the phase transformation from austenite to martensite, there is a region where the strain increases with little or no strain hardening, followed by a region of increased strain hardening (De et al. 2006).

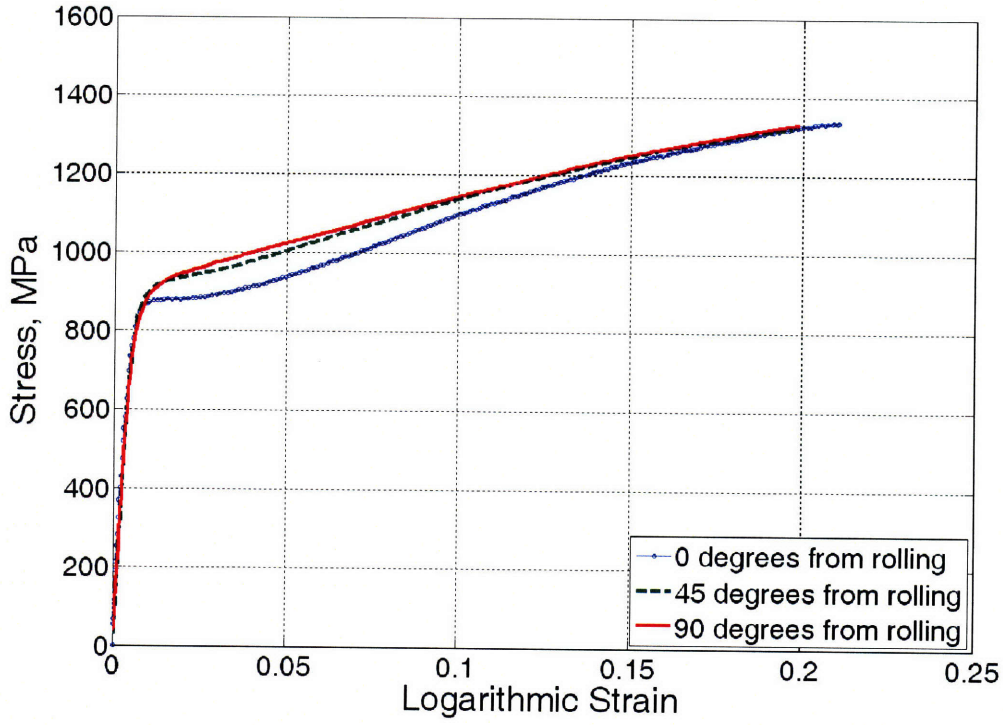

Figure 1: True stress versus true strain for uniaxial tension tests at 0°, 45°, and 90° from the material rolling direction.

The previously mentioned anisotropic yield criteria can accurately capture the differences in initial yield as a function of material direction. However, the evolution of these yield surfaces is either not addressed by these criteria or assumed to be some combination of isotropic and kinematic hardening using an associated flow rule. The models currently included in ABAQUS and LS-DYNA (e.g., Hill 48; Barlat-Lian; Hill 90) include this self-similar hardening, meaning the initial yield values may depend on direction, but the subsequent hardening curves are parallel to each other. Therefore, they differ only by the initial offset. The stainless steel studied in this thesis has differential hardening behavior, meaning that the hardening curves for different material directions are not parallel, but have dissimilar shapes.

Therefore, while the currently implemented models in ABAQUS and LS-DYNA can capture the difference in initial yield, they cannot model the differential hardening.

Clearly, a plasticity model which accurately models the hardening behavior of this material, in terms of isotropic and kinematic hardening, is necessary. Such a model has been developed by Mohr and Jacquemin (2008). This model uses the Hill 48 yield criteria with an associated flow rule to describe the initial yield behavior, but defines a non-associated anisotropic hardening model to describe the subsequent differential hardening behavior. In order to fully characterize the hardening model to relate the plastic strain to the flow stress, a martensitic transformation kinetics law is required. It is the goal of this current thesis and the continuation of this research to develop a martensitic transformation kinetics law that includes the dependence of the martensite content on plastic strain, stress state, and material direction.

Chapter 3: Loading History and Cross Hardening

In many automotive applications, sheet metal is subject to very complex loading histories. During the formation of sheet metal body components, flat metallic sheets are subject to large deformation throughout processes such as stamping or deep drawing. Subsequently, the formed material may be subject to another large deformation history in the event of a vehicle crash. For both forming and crash applications, premature fracture may occur, causing a reduction in the overall structural performance. The prediction of fracture requires detailed knowledge and accurate modeling of the large deformation behavior of the material of interest. At the same time, accurate finite strain plasticity models are very useful in predicting and optimizing the spring back in forming operations as well as in estimating the energy absorption and crash response of automotive structures.

This chapter deals with one specific aspect of the large deformation behavior of austenitic stainless steel sheets. As described in the previous chapter, stainless steel 301LN exhibits anisotropy of the initial yield surface as well as the subsequent hardening curves. The focus of this section is to study the effect of straining in one material direction on the subsequent yield surface in another direction. This effect of the straining in one direction on subsequent strength in another material direction is termed "cross hardening." For instance, uniaxial tension along the specimen's rolling direction is followed by uniaxial tension along the cross-rolling direction, and the difference in strength in these loading steps is examined. The final objective is to characterize the effect of this complex loading on the evolution of the yield surface and the failure properties.

In most sheet metals, anisotropy is introduced during the rolling process in which the induced deformation differs with respect to the rolling direction, the cross direction, and the through-thickness direction. In general, the material grains are elongated in the rolling direction, compressed in the through-thickness direction, and prevented from elongating in the cross direction due to friction between the rollers and the material. This non-uniform deformation results in different mechanical properties in the different

material directions. The yield stresses in different material directions will not be the same, and the strain hardening curves may also differ. In addition to anisotropy introduced by differential deformation depending on material orientation, austenitic steel is also subject to phase transformation from austenite to martensite as a result of deformation. This effect may produce or change preferential directions, and therefore enhance the initial anisotropy in the material.

In the present report, we determine experimentally whether different amounts of initial pre-straining in either the material rolling or cross direction result in different subsequent yield stresses in the material cross or rolling directions, respectively. Furthermore, we focus on the evolution of the yield surface in different material directions to characterize the strain hardening behavior of this material.

3.1 Experimental Procedure

In order to study the effect of cross hardening in 301L stainless steel sheets, the following experimental procedure is performed:

(i) *Preparation of "large" dog bone specimens.* Three large uniaxial tension specimens are cut from both the rolling and the cross-rolling material directions (Figure 2).

(ii) *Pre-straining.* One specimen from each material direction is pre-strained in uniaxial tension to 5%, 10%, or 15% total strain. This strain does not generate diffuse necking, and therefore the strain is uniform in the gauge section of the large specimens. A screw-driven universal testing machine (MTS Model G45) equipped with wedge grips is used to perform these tests.

(iii) *Extraction of "mini" dog bone specimens.* Next, three small uniaxial tension specimens (Figure 3) are machined from each large pre-strained specimen such that the tensile axis of the mini-specimen is perpendicular to the tensile direction of the large specimen. A schematic of the extraction procedure is shown in Figure 4.

(iv) *Tensile testing of mini-specimens.* The mini-specimens are tested to fracture using a hydraulic universal testing machine (Instron Model 8800) with custom-made high precision grips for specimen alignment. It is worth noting

that aligning and securing the mini-specimens is critically important for the overall outcome of this study. Because of the very small gauge section, it is imperative that the specimens are aligned vertically with the tensile axis of the testing machine. It is also important to grip the specimens tightly enough so that they do not slip during loading. When the tests were conducted, a torque wrench was used to apply 80 *Nm* of torque to the bolts holding the grips, however three of the specimens still slipped during loading. When slipping occurred, the test was paused, the grips were tightened further, and the test was resumed.

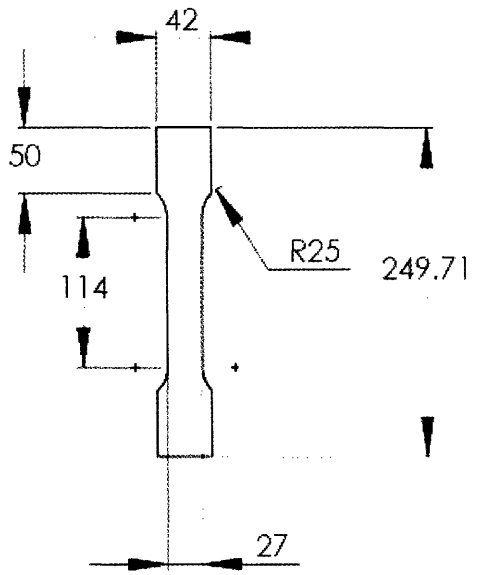

Figure 2: Geometry of large dog bone specimens pre-strained in uniaxial tension (dimensions in *mm*).

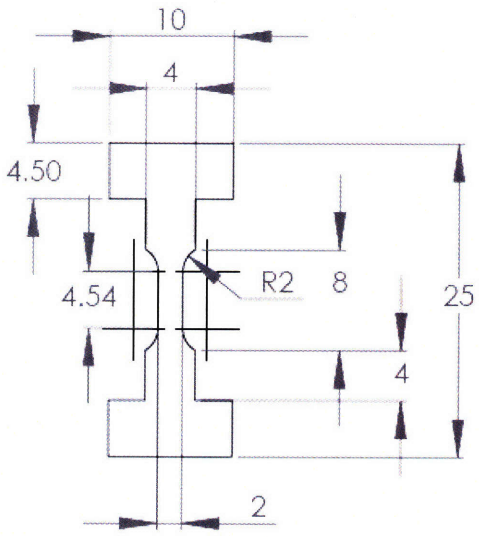

Figure 3: Geometry of mini-specimens cut from large pre-strained specimens (dimensions in *mm*).

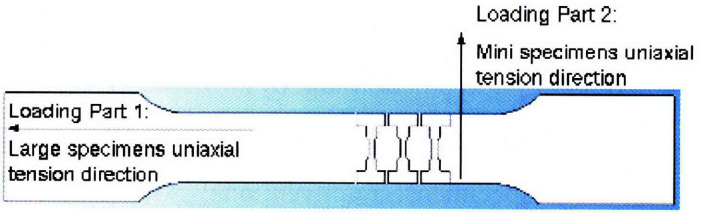

Figure 4: Schematic showing how mini-specimens were cut from large pre-strained specimens.

3.2 Specimen Preparation

The uniaxial tension specimens are designed using the ASME Standard E8M-04 as a guideline for the geometry. The dimensions have been altered slightly to provide an adequate gauge section so that several mini-specimens can be extracted perpendicular to the initial loading direction. The exact geometry of the large specimens is shown in Figure 2. The gauge width of each of the large specimens is 27 *mm*, which allows for the total height of the mini-specimens to be at least 25 *mm* after pre-straining the large specimens to 5% to 15%. The specimens for both stages of the loading program are prepared using a wire Electron Discharge Machine (EDM) with water cooling to

eliminate the possibility of changes in material properties due to temperature concentrations.

3.3 Strain Measurement Technique

The strain fields in the specimens are measured using Digital Image Correlation (DIC). In order to use this technique, a thin layer of white spray paint is applied to the gauge section of each specimen. Subsequently, a random speckle pattern of black spray paint is applied on top of the white paint. This provides a field of dots that can be tracked by the strain DIC algorithm (VIC2D, Correlated Solutions). About 300 images per experiment have been recorded using a monochromatic high resolution digital camera. A virtual two-point extensometer is used to determine the strain histories in both the vertical and the horizontal directions, as shown in Figure 5. The virtual extensometer gauge length is about 3 *mm* for the mini-specimens and 30 *mm* for the large specimens. Based on the placement of the camera, the length of each pixel edge is found to be about 71 μm for the large specimens and 17 μm for the mini-specimens. To determine the displacement fields, a B-spline interpolation algorithm of the Vic-2D software is used. The subset size used to locate the ends of each extensometer is 29 *pixels* by 29 *pixels*.

In the case of the large specimens, a conventional extensometer of 50 *mm* gauge length is also used to obtain real-time measurements of the strain while loading the specimen (note that the DIC strain is usually carried out after completing the experiment). Thus, the experiments can be stopped at the desired pre-strain level.

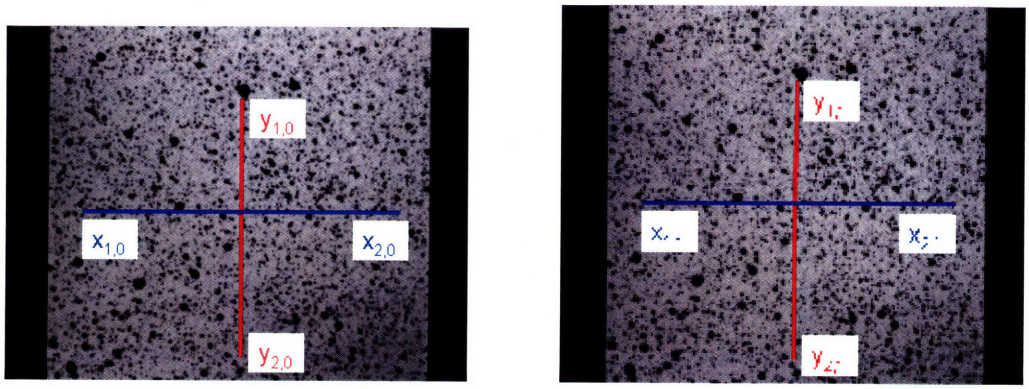

(a) (b)

Figure 5: Vertical and horizontal virtual extensometers in VIC2D at their initial position (a), and final strained position (b).

3.4 Specimen Labeling

The specimens are named according to the following convention:

(1) Large specimens

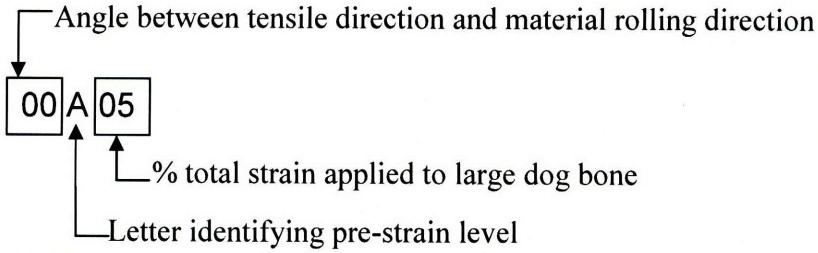

(2) Mini-specimens

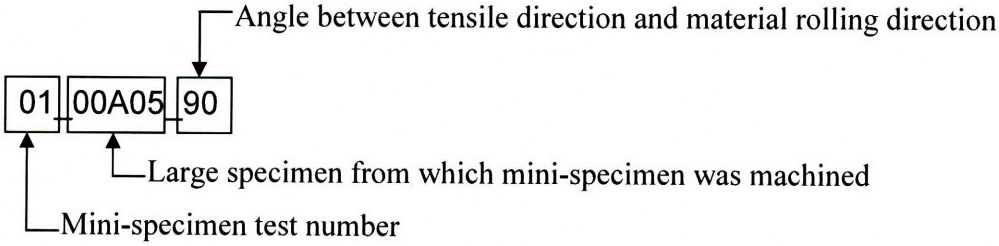

3.5 Determination of Stresses and strains

The stresses are determined using the force output from the MTS machine and the displacement measurements from the optical DIC system. Both engineering and true

stresses and strains are calculated. Note that there are two distinct stages of loading of each material point:

(1) uniaxial tension of a large specimens, followed by

(2) uniaxial tension along a different loading direction of the mini-specimens.

In the following, the strain and stress calculation procedure is outlined in great detail. Special attention is paid to the calculation of the total plastic strains along the rolling and cross-rolling directions.

3.5.1 Loading Stage 1: Uniaxial Tension of the Large Specimens

During the first stage of loading, the engineering strain in the tensile direction, E_1, is defined as

$$E_{1,Stage1} = \frac{\Delta y_{Stage1}}{\Delta y_{0,Stage1}} - 1, \tag{3}$$

where:

$\Delta y_{o,Stage1}$ = initial distance between y_1 and y_2 (pixel coordinates) of the vertical optical extensometer in the digital image correlation for Stage 1

Δy_{Stage1} = distance between y_1 and y_2 (pixel coordinates) defined in digital image correlation for Stage 1

The engineering strain in the width direction, E_2 (perpendicular to the testing direction), is defined as

$$E_{2,Stage1} = \frac{\Delta x_{Stage1}}{\Delta x_{0,Stage1}} - 1, \tag{4}$$

where:

$\Delta x_{o,Stage1}$ = initial distance between x_1 and x_2 (pixel coordinates) of the horizontal optical extensometer in the digital image correlation for Stage 1

Δx_{Stage1} = distance between x_1 and x_2 (pixel coordinates) defined in digital image correlation for Stage 1

The true strain in the tensile direction, ε_1, is defined as

$$\varepsilon_{1,Stage1} = \ln(1 + E_{1,Stage1}) = \ln\left(\frac{\Delta y_{Stage1}}{\Delta y_{0,Stage1}}\right) \tag{5}$$

The true strain in the width direction, ε_2, is defined as

$$\varepsilon_{2,Stage1} = \ln(1 + E_{2,Stage1}) = \ln\left(\frac{\Delta x_{Stage1}}{\Delta x_{0,Stage1}}\right) \tag{6}$$

The engineering stress in the tensile direction, S_1, is defined as

$$S_{1,Stage1} = \frac{F}{A_{o,Stage1}} = \frac{F}{t_{o,Stage1} w_{o,Stage1}}, \tag{7}$$

where:

F = force, *kN*

$A_{o,Stage1}$ = initial cross sectional area, defined as $t_{o,Stage1} w_{o,Stage1}$

$t_{o,Stage1}$ = initial material thickness

$w_{o,Stage1}$ = initial width of gauge section

The true stress in the tensile direction, σ_1, is defined as

$$\sigma_{1,Stage1} = S_{1,Stage1}(1 + E_{1,Stage1}) = \frac{F}{t_{o,Stage1} w_{o,Stage1}}\left(1 + \frac{\Delta y_{Stage1}}{\Delta y_{0,Stage1}}\right) \tag{8}$$

The total strain in the tensile direction during Stage 1 of loading is defined as

$$\varepsilon_1 = \varepsilon_1^e + \varepsilon_1^p = \frac{\sigma_1}{E} - \frac{\nu\sigma_2}{E} - \frac{\nu\sigma_3}{E} + \varepsilon_1^p = \ln\left(\frac{L}{L_o}\right), \tag{9}$$

where:

E = Young's modulus, taken to be 200 *GPa*

ν = Poisson ratio, taken to be 0.3

However, the only non-zero stress is σ_1, so the plastic strain is

$$\varepsilon^p_{1,Stage1} = \varepsilon_{1,Stage1} - \varepsilon^e_{1,Stage1} = \varepsilon_{1,Stage1} - \frac{\sigma_{1,Stage1}}{E} = \ln\left(\frac{\Delta y_{Stage1}}{\Delta y_{0,Stage1}}\right) - \frac{1}{E}\frac{F}{t_{o,Stage1} w_{o,Stage1}}\left(1 + \frac{\Delta y_{Stage1}}{\Delta y_{0,Stage1}}\right) \tag{10}$$

The second principal plastic strain is given by

$$\varepsilon^{p}_{2,Stage1} = \varepsilon_{2,Stage1} - \varepsilon^{e}_{2,Stage1} = \varepsilon_{2,Stage1} + \frac{\nu\sigma_{1,Stage1}}{E} = \ln\left(\frac{\Delta x_{Stage1}}{\Delta x_{0,Stage1}}\right) + \frac{\nu}{E}\frac{F}{t_{o,Stage1}w_{o,Stage1}}\left(1+\frac{\Delta y_{Stage1}}{\Delta y_{0,Stage1}}\right) \tag{11}$$

The assumption of plastic incompressibility gives the third principal strain (through-thickness direction) as

$$\varepsilon^{p}_{3} = -\varepsilon^{p}_{1} - \varepsilon^{p}_{2} \qquad \text{or} \qquad \varepsilon^{p}_{3,Stage1} = -\varepsilon^{p}_{1,Stage1} - \varepsilon^{p}_{2,PStage1} \tag{12}$$

The large uniaxial specimens after initial pre-straining in the rolling or cross-rolling direction to 5%, 10%, or 15% total strain are shown in Figure 6.

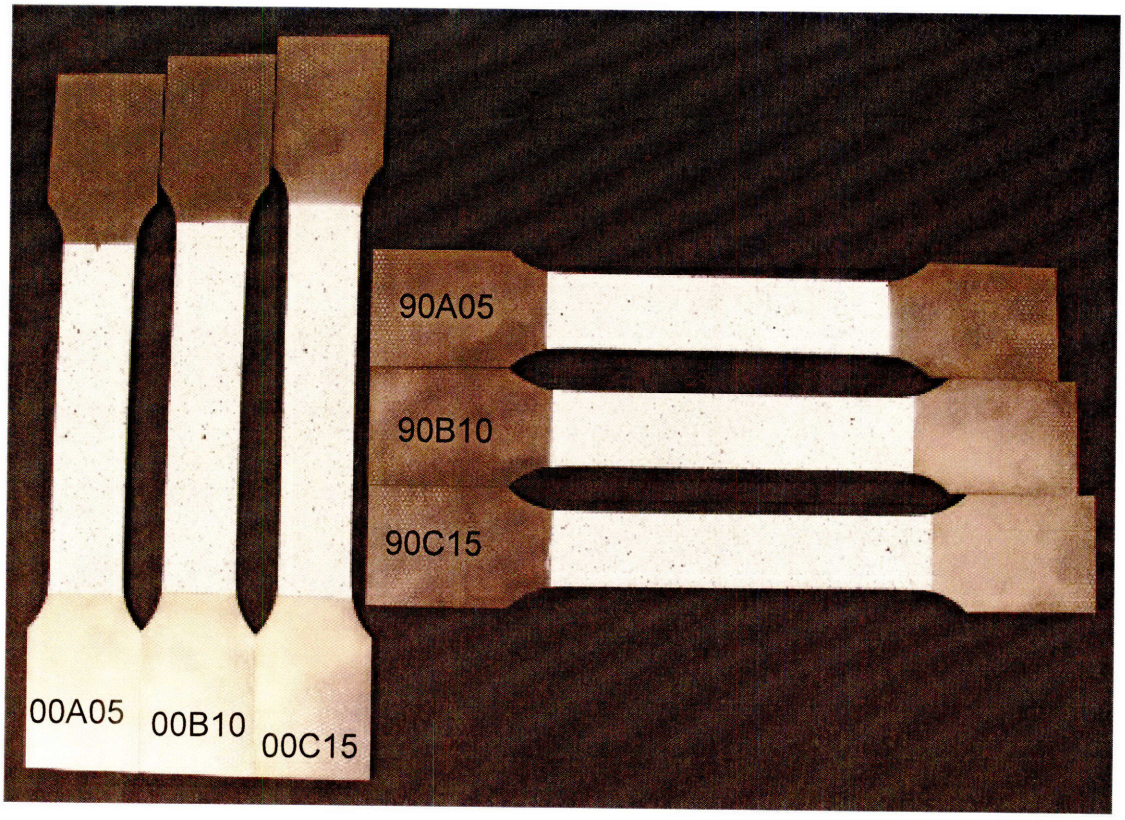

Figure 6: Large dog bone uniaxial tension specimens after Stage 1 of loading.

3.5.2 Loading Stage 2: Uniaxial Tension of the Mini-Specimens

For the second stage of loading, the stresses and strains are calculated for the mini-specimens as described below.

$$E_{1,Stage2} = \frac{\Delta y_{Stage2}}{\Delta y_{0,Stage2}} - 1, \tag{13}$$

where:

$\Delta y_{o,Stage2}$ = initial distance between y_1 and y_2 (pixel coordinates) of the vertical optical extensometer in the digital image correlation for Stage 2

Δy_{Stage2} = distance between y_1 and y_2 (pixel coordinates) defined in digital image correlation for Stage 2

$$E_{2,Stage2} = \frac{\Delta x_{Stage2}}{\Delta x_{0,Stage2}} - 1 \tag{14}$$

Where:

$\Delta x_{o,Stage2}$ = initial distance between x_1 and x_2 (pixel coordinates) of the horizontal optical extensometer in the digital image correlation for Stage 2

Δx_{Stage2} = distance between x_1 and x_2 (pixel coordinates) defined in digital image correlation for Stage 2

The true strains in the tensile direction in Stage 2 loading is defined as

$$\varepsilon_{1,Stage2} = \ln\left(1 + E_{1,Stage2}\right) = \ln\left(\frac{\Delta y_{Stage2}}{\Delta y_{0,Stage2}}\right) \tag{15}$$

The true strain in the width direction in Stage 2 loading is defined as

$$\varepsilon_{2,Stage2} = \ln\left(1 + E_{2,Stage2}\right) = \ln\left(\frac{\Delta x_{Stage2}}{\Delta x_{0,Stage2}}\right) \tag{16}$$

The engineering stress in the tensile direction, $S_{1,Stage2}$, is defined as

$$S_{1,Stage2} = \frac{F}{A_{o,Stage2}} = \frac{F}{t_{o,Stage2} w_{o,Stage2}}, \tag{17}$$

where:

$A_{o,Stage2}$ = initial cross sectional area of mini-specimen, defined as $t_{o,Stage2}w_{o,Stage2}$

$t_{o,Stage2}$ = initial thickness of mini-specimen

$w_{o,Stage2}$ = initial width of mini-specimen gauge section

The true stress in the tensile direction, σ_1, is defined as

$$\sigma_{1,Stage2} = S_{1,Stage2}\left(1+E_{1,Stage2}\right)=\frac{F}{t_{o,Stage2}w_{o,Stage2}}\left(1+\frac{\Delta y_{Stage2}}{\Delta y_{0,Stage2}}\right) \tag{18}$$

The plastic strain in the uniaxial tension direction during Stage 2 of loading is defined as

$$\varepsilon^{p}_{1,Stage2} = \varepsilon_{1,Stage2} - \varepsilon^{e}_{1,Stage2} = \varepsilon_{1,Stage2} - \frac{\sigma_{1,Stage2}}{E} = \ln\left(\frac{\Delta y_{Stage2}}{\Delta y_{0,Stage2}}\right) - \frac{1}{E}\frac{F}{t_{o,Stage2}w_{o,Stage2}}\left(1+\frac{\Delta y_{Stage2}}{\Delta y_{0,Stage2}}\right) \tag{19}$$

The second principal plastic strain during Stage 2 of loading is given by

$$\varepsilon^{p}_{2,Stage2} = \varepsilon_{2,Stage2} - \varepsilon^{e}_{2,Stage2} = \varepsilon_{2,Stage2} + \frac{\nu\sigma_{1,Stage2}}{E} = \ln\left(\frac{\Delta x_{Stage2}}{\Delta x_{0,Stage2}}\right) + \frac{\nu}{E}\frac{F}{t_{o,Stage2}w_{o,Stage2}}\left(1+\frac{\Delta y_{Stage2}}{\Delta y_{0,Stage2}}\right) \tag{20}$$

The third principal strain during Stage 2 of loading is given by

$$\varepsilon^{p}_{3,Stage2} = -\varepsilon^{p}_{1,Stage2} - \varepsilon^{p}_{2,Stage2} \tag{21}$$

The total plastic strain in each material direction is found by calculating the total plastic strain in the rolling and cross directions induced during both Stage 1 and Stage 2 of the loading. Therefore, if pre-straining is done in the rolling direction with subsequent loading in the cross direction, the plastic strains in the material directions are given by:

$$\varepsilon^{p}_{rolling,total} = \varepsilon^{p}_{rolling,Stage1} + \varepsilon^{p}_{rolling,Stage2} = \varepsilon^{p}_{1,Stage1} + \varepsilon^{p}_{2,Stage2} \tag{22}$$

$$\varepsilon^{p}_{cross,total} = \varepsilon^{p}_{cross,Stage1} + \varepsilon^{p}_{cross,Stage2} = \varepsilon^{p}_{2,Stage1} + \varepsilon^{p}_{1,Stage2} \tag{23}$$

If the material is pre-strained in the cross direction and then tested in the rolling direction, the strain definitions are modified accordingly.

3.5.3 Equivalent Plastic Strain

In order to compare the flow strength during the different stages of loading, an equivalent plastic strain measure is used. This allows for the examination of the difference in strength due to different loading paths at the same equivalent plastic strain. A specific form of the equivalent plastic strain depends on the chosen form of the yield function. For example, in the case of the isotropic von Mises yield criteria, the plastic strain is calculated using the following equation:

$$\bar{\varepsilon}^p = \int \sqrt{\left(\frac{2}{9}\right)\left(\left[d\varepsilon_{11}^p - d\varepsilon_{22}^p\right]^2 + \left[d\varepsilon_{22}^p - d\varepsilon_{33}^p\right]^2 + \left[d\varepsilon_{33}^p - d\varepsilon_{11}^p\right]^2\right)} \tag{24}$$

However, as previously discussed, in the plasticity model used to model this material, the Hill 1948 yield criteria is used to describe the initial yield of this material. The equivalent stress of the Hill 1948 yield criterion is given by:

$$\bar{\sigma} = \sqrt{(G+H)\sigma_{11}^2 - 2H\sigma_{11}\sigma_{22} + (F+H)\sigma_{22}^2 + 2N\sigma_{12}^2}\,, \tag{25}$$

where:

$$F = \frac{1}{2}\sqrt{\frac{1}{R_{22}^2} + \frac{1}{R_{33}^2} - \frac{1}{R_{11}^2}} \tag{26}$$

$$G = \frac{1}{2}\sqrt{\frac{1}{R_{11}^2} + \frac{1}{R_{33}^2} - \frac{1}{R_{22}^2}} \tag{27}$$

$$H = \frac{1}{2}\sqrt{\frac{1}{R_{11}^2} + \frac{1}{R_{22}^2} - \frac{1}{R_{33}^2}} \tag{28}$$

By defining the reference stress, σ_o, as the Hill equivalent stress in the 0-degree direction,

$$R_{11} = 1 \tag{29}$$

$$R_{22} = \sqrt{\frac{r_y(r_x+1)}{r_x(r_y+1)}} \tag{30}$$

$$R_{33} = \sqrt{\frac{r_y(r_x+1)}{(r_x+r_y)}} \tag{31}$$

The generalized expression for the equivalent plastic strain corresponding to the Hill 1948 yield function is:

$$\bar{\varepsilon}^p = \int \sqrt{\frac{1}{\alpha}\left[F\cdot\left(d\varepsilon_{11}^p\right)^2 + G\cdot\left(d\varepsilon_{22}^p\right)^2 + H\cdot\left(d\varepsilon_{33}^p\right)^2\right] + \frac{2}{N}\left(d\varepsilon_{12}^p\right)^2} \tag{32}$$

where:

$\alpha = F\cdot G + G\cdot H + H\cdot F$

$d\varepsilon_{11}^p$ = incremental plastic strain in material rolling direction

$d\varepsilon_{22}^p$ = incremental plastic strain in material cross direction

$d\varepsilon_{33}^p$ = incremental plastic strain in through-thickness direction

$d\varepsilon_{12}^p$ = incremental plastic shear strain in plane of sheet

Applying incompressibility and with zero shear stress, Eqn 32 becomes:

$$\bar{\varepsilon}^p = \int \sqrt{\frac{1}{\alpha}\left[F\cdot\left(d\varepsilon_{11}^p\right)^2 + G\cdot\left(d\varepsilon_{22}^p\right)^2 + H\cdot\left(d\varepsilon_{11}^p + d\varepsilon_{22}^p\right)^2\right]} \tag{33}$$

The derivation of Eqn. 32 is presented in Appendix A. For the remainder of this thesis, equivalent plastic strain refers the definition given in Eqn. 32. The above derivation is for materials subjected to tension along the axes of anisotropy. The plastic strain increments are given in terms of material directions, not with respect to directions of tensile loading. Therefore, if a material is subjected to tension along the rolling direction, $d\varepsilon_{11}^p$ is positive and $d\varepsilon_{22}^p$ and $d\varepsilon_{33}^p$ are negative. However if a material is subjected to uniaxial tension in the cross-rolling direction, $d\varepsilon_{22}^p$ corresponds to the tensile direction and therefore is positive while $d\varepsilon_{11}^p$ and $d\varepsilon_{33}^p$ are negative. This is further demonstrated by the following:

When testing in the material rolling direction, "r_0" is given by Eqn. 1 as

$$r_0 = \frac{d\varepsilon_{22}}{d\varepsilon_{33}} = \frac{-d\varepsilon_{22}}{d\varepsilon_{11} + d\varepsilon_{22}} = 0.6$$

Rearranging this to obtain an expression for the equivalent plastic strain only in terms of $d\varepsilon_{11}^p$ gives:

$$d\varepsilon_{22} = \frac{-d\varepsilon_{11}}{1 + 1/r_0}$$

Using incompressibility and not considering shear strains, Eqn. 32 for loading in the material rolling direction becomes:

$$\bar{\varepsilon}^p = \int d\varepsilon_{11}^p \sqrt{\frac{1}{\alpha}\left[F + H + \frac{G+H}{(1+1/r_0)^2} - \frac{2H}{(1+1/r_0)}\right]} \tag{34}$$

The plastic strain increment corresponding to the uniaxial tensile load when applying tension in the cross rolling direction is $d\varepsilon_{22}^p$, so $d\varepsilon_{11}^p$ is given as:

$$d\varepsilon_{11} = \frac{-d\varepsilon_{22}}{1 + 1/r_{90}}$$

Again using incompressibility and not considering shear strains, Eqn. 32 for loading in the material cross-rolling direction becomes:

$$\bar{\varepsilon}^p = \int d\varepsilon_{22}^p \sqrt{\frac{1}{\alpha}\left[\frac{F+H}{(1+1/r_{90})^2} + G + H - \frac{2H}{(1+1/r_{90})}\right]} \tag{35}$$

The anisotropy parameters F, G, and H are invariant. With $r_x = r_0 = 0.6$ and $r_y = r_{90} = 0.8$, F = 0.47, G = 0.63, and H = 0.38. Eqns. 33 and 34 are given to illustrate how the loading history is taken into account in terms of the Hill 1948 anisotropic coefficients. However, in calculation of the equivalent plastic strains, $d\varepsilon_{11}^p$ and $d\varepsilon_{22}^p$ will be explicitly measured during the experiments, and the form for equivalent plastic strain given Eqn. 33 will be used. The total equivalent plastic strain in the specimen during Stage 2 is calculated by:

$$\bar{\varepsilon}^p = \bar{\varepsilon}_{Stage1}^p + \bar{\varepsilon}_{Stage2}^p \tag{36}$$

3.5.4 Yield Stress

Yield stresses are measured by two methods. The first method (Method 1) involves taking the stress measurement at 0.2% plastic strain in Stage 1 of testing, or 0.2% plastic strain during Stage 2 of testing, assuming no initial plastic deformation. This is the typical method used in mechanics for defining the yield stress; however, due to the nonlinearity of the stress-strain curve, this measurement may give a relatively low value for yield stress, and not indicate when the material loses its stiffness. The preferred method (Method 2) involves taking the tangent of the stress-plastic strain curve at 2% plastic strain and extrapolating this line back to zero plastic strain. To calculate the yield in Stage 2 of loading, the tangent line is taken at an additional 2% plastic strain from the plastic strain introduced during the initial pre-strain and extrapolated back to the previous level of plastic strain. This method is illustrated in Figure 7.

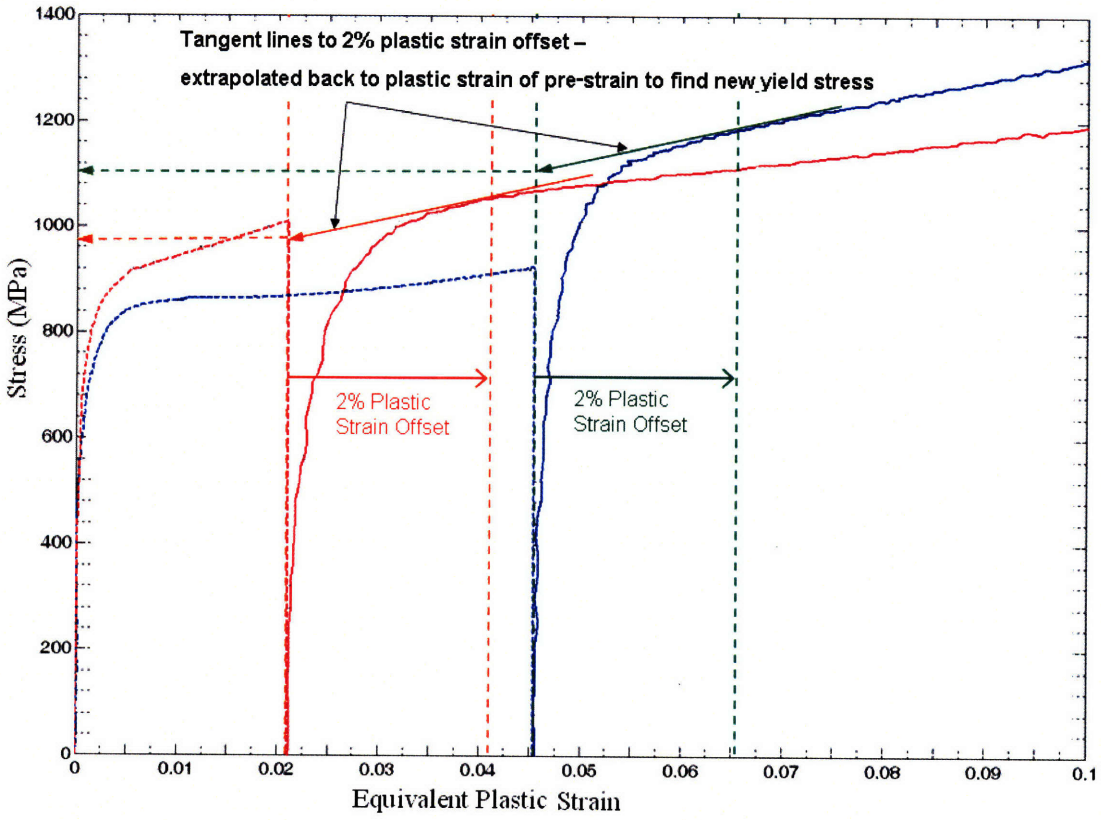

Figure 7: Illustration of Method 2 for determining yield stress.

3.6 Experimental Results

The experimental results produced during the initial pre-straining are shown in Figure 8. The experimental results produced during Stage 2 of loading are plotted in several ways as discussed below.

3.5.5 Loading Stage 1: Large Dog Bone Specimens

The large dog bone specimens are strained to a total engineering strain of 5%, 10%, and 15%. The total strain and plastic strain induced during Stage 1 of the loading are shown in Table 1. The loading conditions and resulting strain rates are reported in Table 2. The measured true stress versus true strain curves are shown in Figure 8. The comparison of the curves for the same loading direction indicates a good repeatability of the experimental results. Uniaxial tension tests were also performed on the same material independently by Mohr and Jacquemin (2008). Their results (shown as dashed lines in Figure 8) are in good agreement with the results produced by the present six tests.

Table 1: Percent strain induced in specimens during Stage 1 loading (large dog bone specimens) and final flow stresses during pre-straining.

Specimen	Total strain	Plastic strain induced in tensile direction	Plastic strain induced in direction perpendicular to tensile loading	Flow stress, *MPa*
00A05	5.0	4.5	-1.7	923.2
00B10	10.0	9.5	-3.7	1095.5
00C15	15.4	14.7	-5.9	1256.3
90A05	5.2	4.7	-2.1	1010.8
90B10	10.3	9.7	-4.4	1147.2
90C15	15.2	14.6	-6.6	1259.4

Table 2: Applied loading rate and subsequent strain rates during Stage 1 loading.

Specimen	Loading rate (*mm/min*)	Logarithmic strain rate in tensile direction
00A05	1	1.4E-04
00B10	2	4.7E-04
00C15	3	6.7E-04
90A05	1	2.7E-04
90B10	2	5.2E-04
90C15	3	7.5E-04

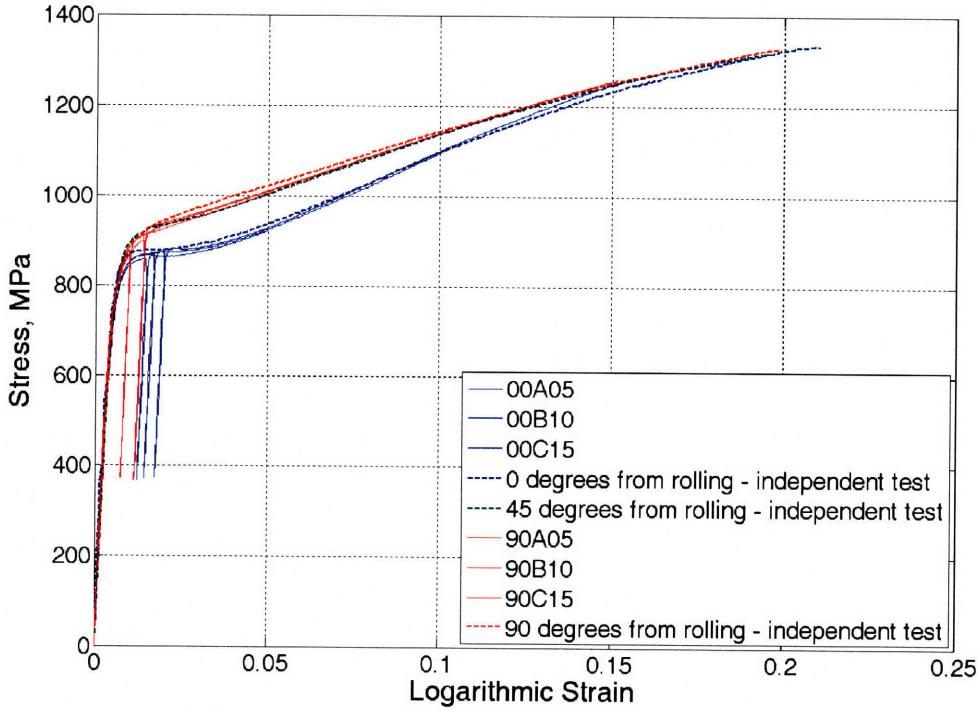

Figure 8: True stress versus true strain for large uniaxial tension tests at 0°, 45°, and 90° from the material rolling direction.

3.5.6 Loading Stage 2: Mini-Specimens

In Stage 2, the mini-specimen tension tests, which are performed perpendicular to the pre-strain tensile direction, are carried out all the way to fracture. It can be seen from the

curves shown in Figure 9 and Figure 10 that the tests of specimens pre-loaded in the rolling direction and subsequently tested in the cross direction produced more repeatable results than those tested in the opposite order. As previously mentioned, alignment of the mini-specimens is critical because of the small gauge section. Therefore, the fact that these tests results are not extremely repeatable may be attributed to slight misalignment of the specimens. In addition, the mini-specimens were cut from the gauge section of the large specimens. To allow for leftover material for subsequent tests, mini-specimens were cut from one end of the large specimen. Although initially it was presumed that the mini-specimens were cut far enough away from the end of the large specimens, some specimens may have been cut too close to the shoulder region of the large specimens, in a region where the initial pre-strain was not completely uniform. This would result in a different initial pre-strain in the mini-specimens and also, perhaps, a non-uniform pre-strain field in specimens cut close to the shoulder regions, and would contribute to decreasing the repeatability of the tests.

Three-dimensional graphs are shown in Figure 11 to illustrate the dependence of stress on the total plastic strain in the respective material directions. This plot shows the stress versus plastic strain in the rolling direction and the plastic strain in the cross direction for each of the tests. Specifically, it shows that during pre-straining in the cross direction, a negative plastic strain is induced in the rolling direction and a positive plastic strain is induced in the cross direction. Subsequent straining in the rolling direction introduces positive plastic strain in the rolling direction and negative plastic strain in the cross direction. It serves to illustrate the loading history of each specimen. The stress-strain plots are only shown to the point of necking, which preceded fracture in each of the tests in Stage 2 loading.

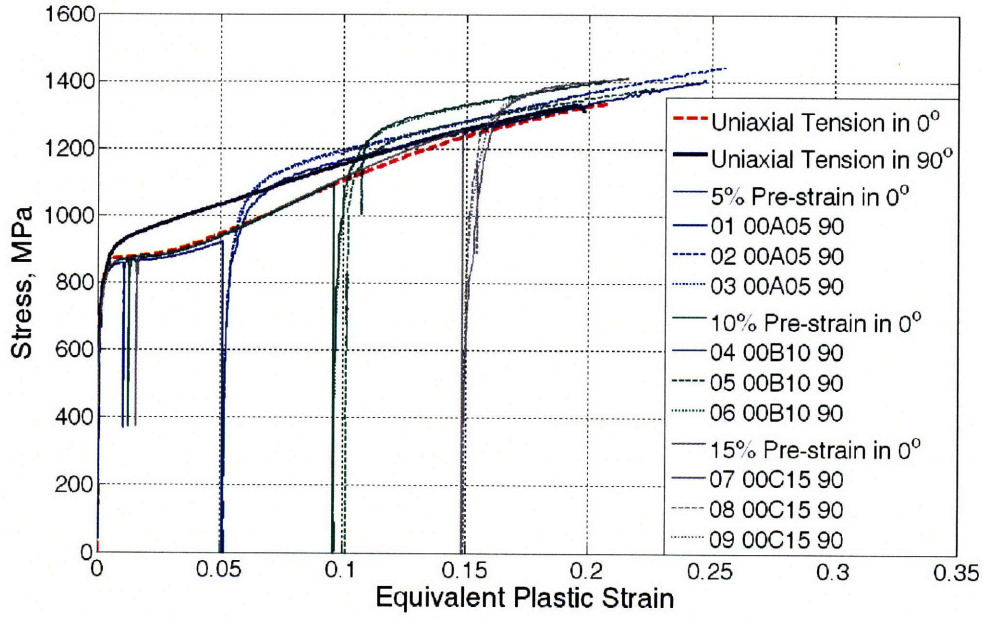

Figure 9: True stress versus equivalent plastic strain for tests pre-strained in the material rolling direction and then tested in the cross direction.

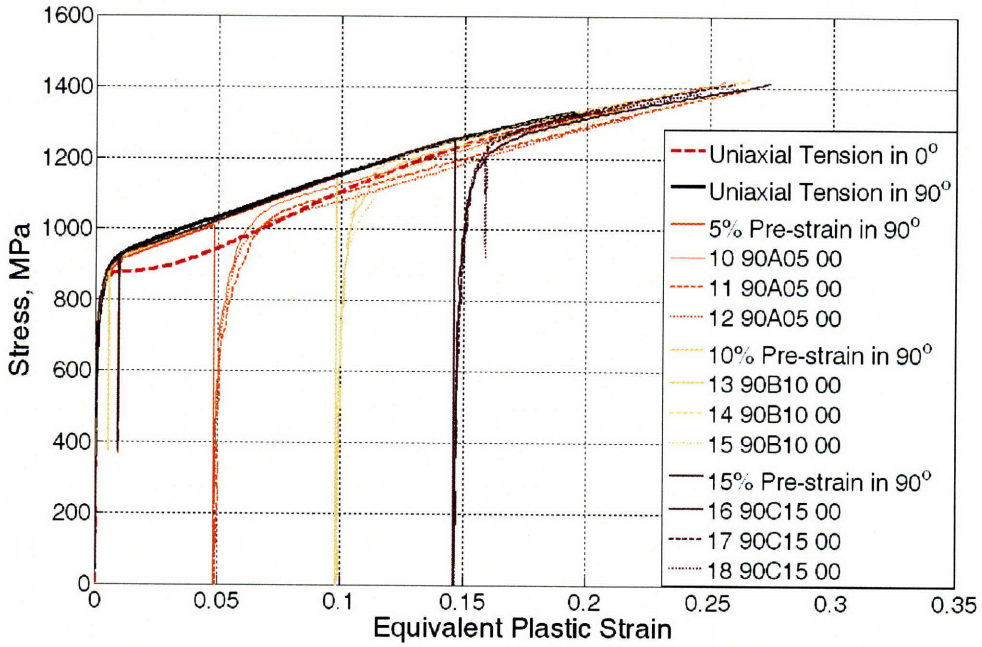

Figure 10: True stress versus equivalent plastic strain for tests pre-strained in the material cross direction and then tested in the rolling direction.

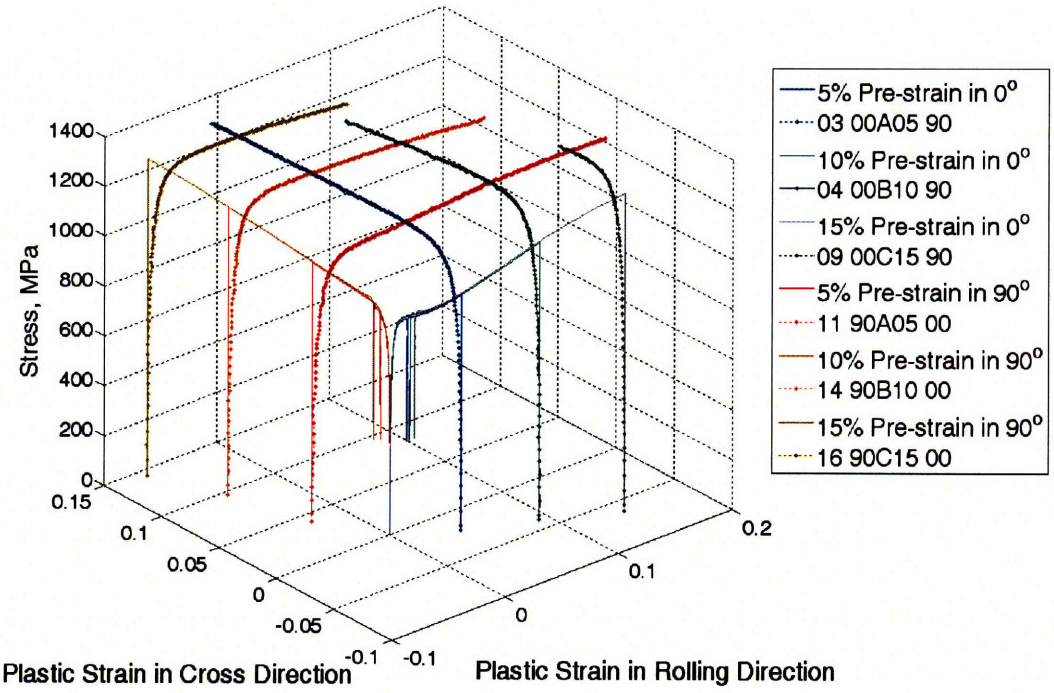

Figure 11: True stress versus plastic strain for large uniaxial tension tests at 0° and 90° from the material rolling direction followed by uniaxial tension tests on mini-specimens at 90° and 0° from the material rolling direction, respectively. This plastic strain is separated as the accumulated plastic strain in the rolling direction and the accumulated plastic strain in the cross-rolling direction as a result of Stage 1 and Stage 2 loading.

3.7 Cross Hardening Effects

In order to determine the effect of loading in one direction on subsequent flow strength in another direction, the stress histories are compared using the equivalent plastic strain as a reference axis. Table 3 provides the flow stress at various levels of plastic strain that are used as reference values with which to compare the flow stress in the pre-strained specimens. Table 4 gives the percent increase in flow strength at the end of the pre-strain experiment to the yield stress observed at the beginning of the subsequent Stage 2 loading. More specifically, it compares the final flow stress observed during pre-straining in the rolling direction with the subsequent yield stress in the cross direction. It shows that once the material is pre-strained in the rolling direction, there is a resulting

increase in yield stress when it is subsequently tested in uniaxial tension along the cross direction. Using Method 2 for defining the yield stress, and comparing the initial yield to the final flow stress in the rolling direction, the flow stress for uniaxial loading along the cross direction *increases* by

- 14% in the specimens pre-strained 5% in the rolling direction,
- 6% in the specimens pre-strained 10% in the rolling direction, and
- 1% in the specimens pre-strained 15% in the rolling direction.

When a specimen is pre-strained in the cross direction and then subjected to uniaxial tension in the rolling direction, the yield stress (by Method 2) decreases from the reference flow strength. The initial yield stress along the rolling direction, as compared to the final flow stress along the cross direction, *decreases* on average by

- 9% when the material is pre-strained 5% in the cross-rolling direction,
- 7% when the material is pre-strained 10% in the cross-rolling direction, and
- 6% when the material is pre-strained 15% in the cross-rolling direction.

A more suitable comparison is made between the flow stresses in the same material directions and at the same equivalent plastic strain. The initial yield stress of a mini-specimen being strained in the material rolling direction is compared to the yield stress in a uniaxial tension test in the rolling direction at the same equivalent plastic strain level that is induced in Stage 1 loading of the large dog bone specimen from which the mini-specimen is extracted. As seen in Table 5, on average, the yield stress in the cross-rolling direction increases by about 2% when pre-straining in the rolling direction. This increase in flow stress is almost independent of the amount of pre-strain introduced during Stage 1 loading. To summarize, the flow strength for uniaxial tension in the cross-rolling direction, after pre-straining in the rolling direction, *increases* by the following amounts as compared to the flow strength at the same equivalent plastic strain for a specimen tested only in the cross direction:

- 4% in the specimens pre-strained 5% in the rolling direction,
- 2% in the specimens pre-strained 10% in the rolling direction, and
- 1% in the specimens pre-strained 15% in the rolling direction.

Conversely, the initial yield stress in the rolling direction decreases slightly after 5% strain in the cross direction, and the degradation of strength increases with increasing

pre-strain in the cross direction. When the steel is pre-strained 5% in the cross direction and then tested in the rolling direction, it retains roughly the same yield stress as if it were under uniaxial tension in the rolling direction at 5% total strain. The flow strength for uniaxial tension in the rolling direction, after pre-straining in the cross direction, *decreases* by the following amounts as compared to the flow strength at the same equivalent plastic strain for a specimen tested only in the rolling direction:

- 0% when the material is pre-strained 5% in the cross-rolling direction,
- 2% when the material is pre-strained 10% in the cross-rolling direction, and
- 6% when the material is pre-strained 15% in the cross-rolling direction.

Upon further investigation of the values in Table 5, it is noted that with increasing pre-strain in the rolling direction, subsequent uniaxial tension in the cross direction tends to approach the corresponding yield stress for uniaxial tension in the cross direction. Thus, the difference between yield stress in the material that has been pre-strained and material tested only in the cross-rolling direction becomes smaller as the amount of pre-strain in the rolling increases. However, the opposite is true of material pre-strained in the cross-rolling direction and then tested in the rolling direction. With increasing pre-strain in the cross-rolling direction, the subsequent uniaxial tension in the rolling direction deviates further from the corresponding yield stress for uniaxial tension in the rolling direction. Figure 9 shows true stress versus equivalent plastic strain for specimens pre-strained in the rolling direction and then tested in the cross direction. It can be seen that the yield stress of material pre-strained and tested in this order jumps above the uniaxial curve for monotonic loading in both the rolling and cross directions. However, as shown in Figure 10, the hardening curve for specimens pre-strained in the cross-rolling direction and then tested in the rolling direction more closely follows the curve for uniaxial tension in the rolling direction or undershoots the hardening curves for monotonic loading in both the rolling and cross-rolling directions. Therefore, pre-straining in the cross-rolling direction appears to have less of an effect on the hardening curve in the rolling direction, while pre-straining in the rolling direction increases the hardening curve for subsequent loading in the cross-rolling direction.

Table 3: Flow stress for uniaxial tension loading at 5%, 10%, and 15% total strain (the levels of pre-straining) for comparison of subsequent yielding in these material directions.

% Total Strain	Flow Stress (*MPa*) in Rolling Direction, 0^{o}	Flow Stress (*MPa*) in Cross Direction, 90^{o}
5	925	1011
10	1095	1147
15	1256	1259

Table 4: Comparison between final flow stress (in *MPa*) during pre-strain and subsequent yielding (using Method 2) during uniaxial tension in the perpendicular material direction. Comparison is made between final flow stress in material after pre-straining and the subsequent yield stress in the same material (but different material direction).

Test Number	Yield calculated by Method 2 (extrapolated at tangent at 2% $\bar{\varepsilon}^{p}$)	Percent increase over flow stress in pre-strained specimen
01_00A05_90	1025	10.8
02_00A05_90	1045	13.0
03_00A05_90	1085	17.3
Average 00A05_90	**1052**	**14**
04_00B10_90	1160	5.9
05_00B10_90	1155	5.5
06_00B10_90	1180	7.8
Average 00B10_90	**1165**	**6**
07_00C15_90	1320	5.1
08_00C15_90	1220	-2.9
09_00C15_90	1280	1.9
Average 00C15_90	**1273**	**1**
10_90A05_00	950	-6.0
11_90A05_00	890	-12.0
12_90A05_00	925	-8.5
Average 90A05_00	**922**	**-9**
13_90B10_00	1050	-8.5
14_90B10_00	1125	-1.9
15_90B10_00	1040	-9.3
Average 90B10_00	**1072**	**-7**
16_90C15_00	1185	-5.9
17_90C15_00	1185	-5.9
18_90C15_00	1175	-6.7
Average 90C15_00	**1182**	**-6**

Table 5: Comparison between final yield stress (in *MPa*) during pre-strain and subsequent yielding (using Method 2) during uniaxial tension in the perpendicular material direction. Comparison is made only between stresses in the same loading direction.

Test Number	Yield calculated by Method 2 (extrapolated at tangent at 2% $\bar{\varepsilon}^{p}$)	Percent increase in flow stress (compared to σ_y in same material direction at same pre-strain from Table 3)
01_00A05_90	1025	1.4
02_00A05_90	1045	3.4
03_00A05_90	1085	7.3
Average 00A05_90	**1052**	**4**
04_00B10_90	1160	1.1
05_00B10_90	1155	0.7
06_00B10_90	1180	2.9
Average 00B10_90	**1165**	**2**
07_00C15_90	1320	4.8
08_00C15_90	1220	-3.1
09_00C15_90	1280	1.7
Average 00C15_90	**1273**	**1**
10_90A05_00	950	2.7
11_90A05_00	890	-3.8
12_90A05_00	925	0.0
Average 90A05_00	**922**	**0**
13_90B10_00	1050	-4.1
14_90B10_00	1125	2.7
15_90B10_00	1040	-5.0
Average 90B10_00	**1072**	**-2**
16_90C15_00	1185	-5.7
17_90C15_00	1185	-5.7
18_90C15_00	1175	-6.4
Average 90C15_00	**1182**	**-6**

3.8 Conclusions

The hardening behavior of stainless steel 301L has been studied. The main experimental observations are:

(1) Pre-straining a specimen in the material rolling direction and then subjecting it to tension in the cross direction results in an increase in the yield strength from both (a) the previous flow strength of the same specimen in the rolling direction and (b) a specimen at the same equivalent plastic strain subjected to uniaxial tension in the cross direction. Comparing the initial yield of the mini-specimen to the flow strength of material in the cross direction at the same equivalent plastic strain, the increase in strength is about 4% when subjected to 5% pre-strain. However, this improvement in flow strength decreases with increasing pre-strain in the rolling direction, and the improvement in flow strength decreases to 1% when the specimen is pre-strained 15% in the rolling direction. The same general trend is observed when comparing the flow strength in the same specimen – the increase in flow strength in the specimen is highest when the specimen is subjected to 5% pre-strain in the rolling direction, and this increase in strength decreases with increasing pre-strain.

(2) Pre-straining a specimen in the cross direction and then subjecting the specimen to tension in the rolling direction results in a degradation in the subsequent yield stress as compared with the previous flow strength of the material in the same specimen in the cross direction. The degradation in flow strength is 9% when the pre-strain in the cross-rolling direction is 5%. This degradation decreases with increasing strain so that when the pre-strain is 15%, the flow strength decreases 6%. However, when comparing the initial yield of the mini-specimens with the flow strength in the rolling direction at the same equivalent plastic strain, the strength is about the same with 5% pre-strain in the cross direction, but as the pre-strain increases, the degradation in flow strength increases.

Therefore, it may be concluded that pre-straining in the rolling direction increases the material strength in the cross direction, while pre-straining in the cross direction, has a negative effect on the subsequent yield in the rolling direction.

Chapter 4: Quantification of Martensite Evolution

In order to more accurately describe the macroscopic plasticity behavior of this stainless steel, a martensitic transformation kinetics law describing the transformation's dependence on material anisotropy and stress state must be developed and integrated into the existing plasticity model. This thesis discusses studies that were performed to quantify the level of martensite present in the stainless steel at various stages of loading. The three methods used for this measurement are X-ray diffraction, micrography, and implementation of a magnetic induction method. The X-ray diffraction and micrography measurements required interrupted tests, while the magnetic induction method allowed for in-situ measurements with a Fischer Feritscope MP30.

4.1 X-Ray Diffraction Study

X-ray diffraction is used to determine the amount of BCC-martensite versus FCC-austenite present in the original cold-rolled steel as well as in two samples that were subjected to a prescribed amount of plastic strain. X-ray diffraction exploits Bragg's law of diffraction to determine the crystal structures present in the specimen.

4.1.1 Description of X-Ray Diffraction Measurement Technique

X-ray diffraction involves irradiating a volume element of a sample; in this case, the area studied is on the surface of the gauge section of a stainless steel 301LN mini-specimen. The X-rays are then scattered back constructively when Bragg's law of diffraction, which depends on the distance between crystal planes as well as the difference between the angle of incidence and the scattering planes, is satisfied. Bragg's law is given by:

$$n\lambda = 2d \cdot \sin\theta \tag{37}$$

Where:

n = an integer

λ = wavelength of the incident X-ray beam

d = distance between the planes in the atomic crystal lattice

θ = angle between the incident ray and the scattering planes

Depending on the chemical composition of the specimen being irradiated as well as its crystal structure, a unique diffraction pattern will be detected by the machine. The underlying assumption when using X-ray diffraction to determine the chemical composition or crystal structures present in a sample is that the volume being irradiated is composed of thousands of randomly oriented grains. Therefore the sample has no preferred orientation, referred to as texture. If this is the case, the X-ray diffraction scan should detect a statistical representation of the crystal structure present in the sample. The resulting unique diffraction pattern can be matched with a large database of the diffraction patterns of various crystal structures of numerous of chemical compositions.

Several angles are used to define the relative location of the X-ray beam and the sample orientation. These are illustrated in Figure 12. The angle between the incident X-ray beam and the diffracted beam is 2θ. In the systems used in this study, the X-ray tube is fixed, and changes in diffraction angles are measured by moving the detector in an arc along 2θ. The angle 2θ is independent of the sample. The equatorial plane is the plane that contains the vector of the incident X-ray beam and the arc of motion of the detector. The three directional axes of the sample are subsequently defined as follows: z is the outward normal of the sample's surface; x is the orthogonal direction that lies within the equatorial plane; and y is the orthogonal direction normal to the equatorial plane. The final three angles, which can be adjusted, are rotations about the sample. Chi (χ) is rotation about the x-axis, and is called the tilt axis. Omega (ω) is rotation about the y-axis and determines the incident angle of the X-ray hitting the sample. Phi (φ) is rotation about the z-axis, and is called the rotation axis. In a non-textured sample, which is comprised of thousands of randomly oriented grains, the intensity of a peak at angle 2θ is independent of the angles ω, φ, and χ. However, the samples examined in this study have significant texture based on the fact that the intensity of any diffraction peak at an angle 2θ varies when the angles of ω, φ, and χ are changed.

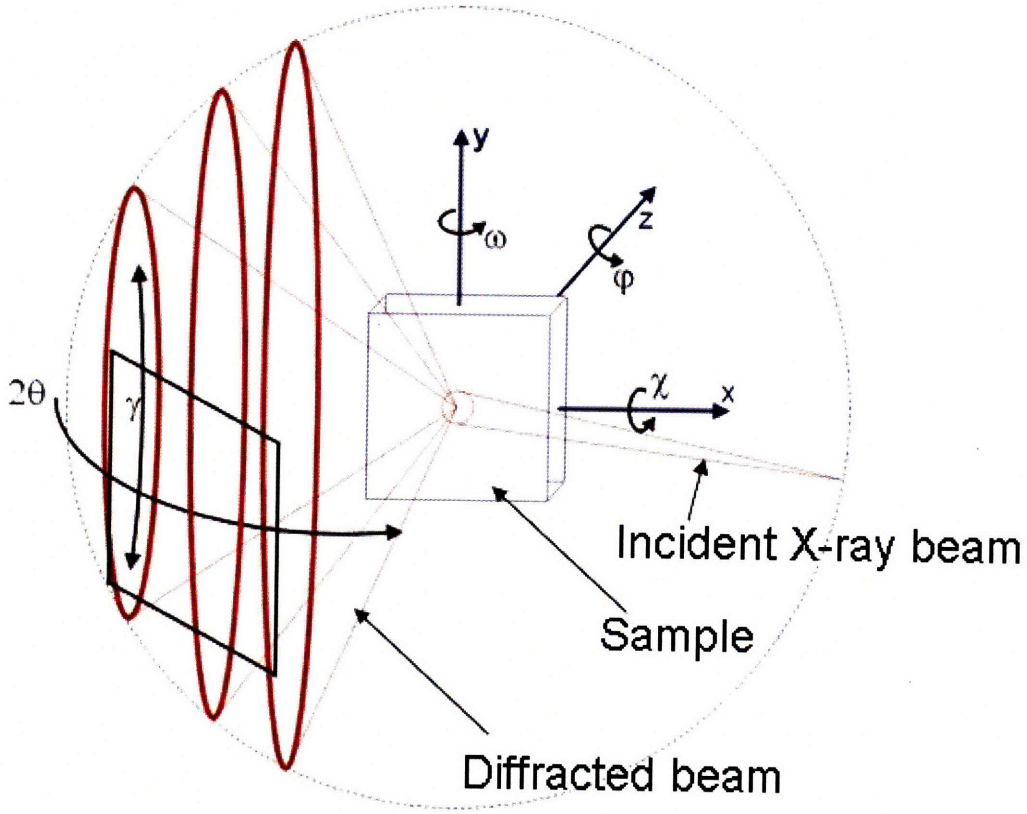

Figure 12: Schematic to define angles in X-ray diffraction analysis (figure made by Dr. Scott Speakman).

The texture effect, noted with the variation of χ, produces difficulty in that it violates the underlying X-ray diffraction assumption of totally random crystals. This problem is addressed in several ways during the present analysis in order to decrease texture effects on the predicted crystal structure of the samples, but it cannot be completely eliminated or ignored.

It is also important to recognize the volume of material that can be analyzed in X-ray diffraction analysis. The depth of material that the X-rays can irradiate depends on material properties of the sample being examined, namely the mass absorption coefficient and the bulk density, as well as the incident angle and wavelength of the X-ray beam. In this study, two different X-ray diffraction machines are used. The depth of penetration

was determined to be between 4 and 13 μm, which results in an irradiated volume of approximately 0.064 mm^3 for the PANalytical machine and 0.004 mm^3 for the BruckerD8.

4.1.2 Preparation of Specimens

Three mini-specimens are machined using wire EDM from the original sheet material, with the geometry shown in Figure 3. The first specimen is machined directly from the original sheet, and is called the "original" specimen. The second specimen, called the "rolling" specimen, is machined with its tensile axis aligned with the material rolling direction, and strained to a plastic strain of 15% along the material rolling direction. The third specimen, called the "cross" specimen, is machined with its tensile axis aligned with the material cross direction, and strained to a plastic strain of 15% along the material cross direction.

4.1.3 X-Ray Diffraction Analysis

Two different machines are used for the X-ray diffraction analysis. The first machine used is a Bruker D8 diffractometer with general area detector diffraction system (GADDS) that simultaneously collects data over a range of 30 degrees 2θ and 30 degrees χ. This detector range allows a portion of the arc from multiple Debye rings to be observed simultaneously. The diameter of the area examined is about 0.5 mm. First, the specimen is examined over a 2θ range of about 30° while the specimen is rotating about the z-axis. The purpose of this scan is to collect as much data as possible from different grains during the analysis to get an initial idea of the phases present in the specimen. The resulting image shows a series of continuous Debye rings, where each ring indicates the presence of one or more phases. Then a scan is performed with a 2θ of 30° at a tilt of 0°, 15°, and 30° with the specimen stationary in order to determine if the specimen is strongly textured. A continuous Debye ring in these scans would indicate little to no texture present in the specimen, meaning that the grains in the specimen are randomly aligned. However, the observed Debye rings show varying intensity along the same ring, indicating that there is significant texture present. All of the samples exhibit texture: the original sample is the least textured and the rolled sample is the most textured.

Subsequent analysis is done on a PANalytical X-Pert Pro Multipurpose Diffractometer, to take more accurate, longer scans. Wobble scans are done on the three specimens so that the χ tilt of the specimen is effectively increased 1° between each analysis, thereby examining a 5° χ tilt range in five different scans. This wobble scan is used as an attempt to decrease the texture effects from the measurement by taking data from multiple values of χ and adding all of the resulting diffraction patterns together to even out the intensities. However, a range of χ of 5° is not as large as the range observed using the Bruker D8 machine, and the 5° variation cannot completely eliminate the texture effects. The resulting intensities for the five scans for each specimen are then added to each other to increase the overall data to be measured (i.e., the five scans for the original material are added to each other; the five scans for the rolling specimen are added to each other; and the five scans for the cross specimen are added to each other). The resulting scans are shown in Figure 13.

Background noise is observed in each of the scans. The background level is consistent in each of the scans, and is due to the fact that iron both absorbs and fluoresces the copper radiation wavelength. This has a twofold effect of (1) decreasing the reflected intensities, because some X-rays are absorbed instead of diffracted, and (2) reflecting back the fluoresced radiation as background noise. These effects combine to produce a weaker diffraction signal with a noisier background. The background noise is present in the resulting scan shown in Figure 13. However, the noise is removed from the intensity measurements by modeling the background in the analysis, and eliminating the background contribution to the observed peak intensity.

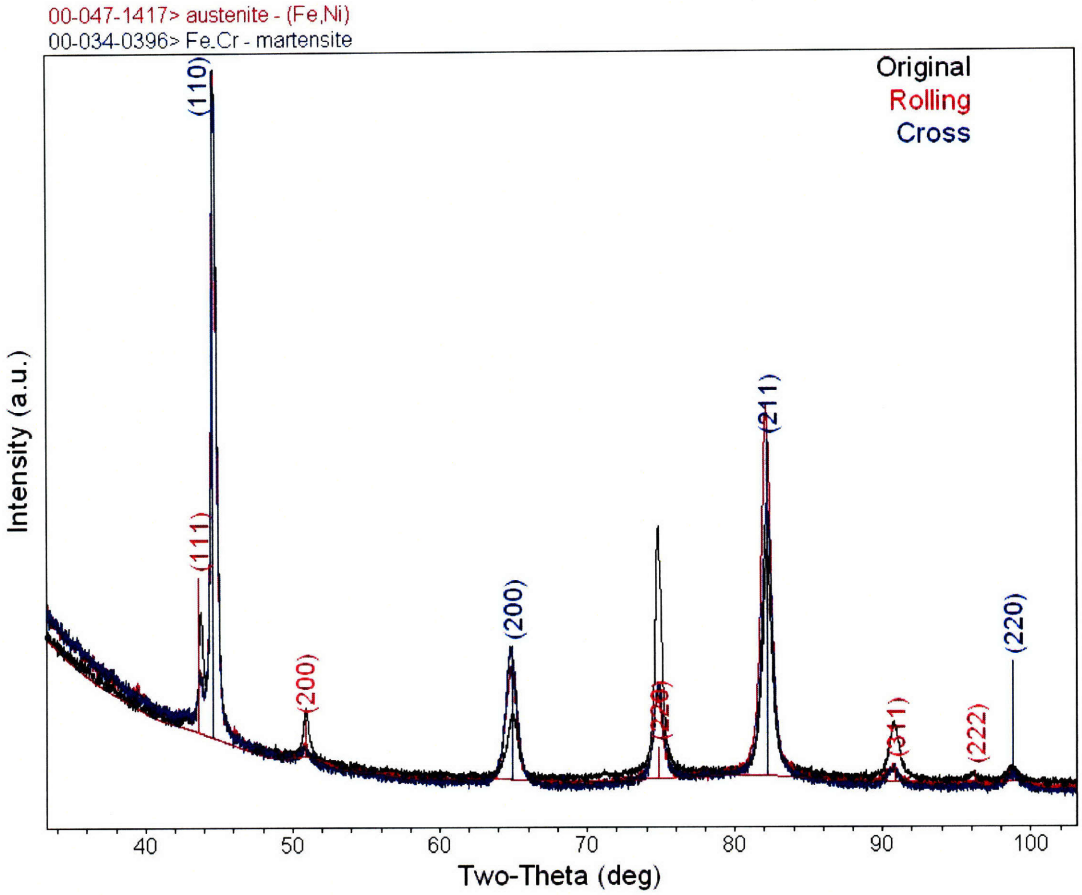

Figure 13: X-ray diffraction scans of three different specimens showing the presence of γ–austenite and α'-martensite. The three scans shown are for the original material (black), the specimen strained to 15.9% in the rolling direction (red), and the specimen strained to 15.7% in the cross direction (blue).

4.1.4 X-Ray Diffraction Results

Two different methods are used to analyze the resulting data. The first method employs the Reference Intensity Ratio method, a semi-qualitative analysis, which uses the intensity of individual peaks from different phases to determine the relative amount of each phase. The second method uses a computer software package to model the texture of the specimen by using Whole Pattern Fitting, which aims to ensure that the entire

diffraction pattern is fitted to account for any possible preferred orientation. The second method provides a more rigorous approach.

4.1.4.1 Analysis Method 1: Reference Intensity Ratio method

The first method used to analyze the resulting data follows the general procedure outlined in ASTM Standard E975-03 to determine the amount of austenite versus the amount of martensite in the specimens. Integrated areas under each peak are used to determine the intensity of each peak. The Reference Intensity Ratio (RIR) method is used (Jenkins and Snyder 1996) to determine the mass fractions of austenite and martensite. Each RIR gives the ratio of the maximum peak intensity of the crystal of interest to the reference peak of corundum in a 1:1 mixture of the two compounds. The RIR of FCC pure iron is 7.97, while the RIR of BCC pure iron is 10.77. The following calculation is performed to determine the fraction of weight percentages of martensite to austenite in the material:

$$\frac{X_\gamma}{X_{\alpha'}} = \frac{RIR_\gamma}{RIR_{\alpha'}} \cdot \frac{I_{\alpha',observed}}{I_{\gamma,observed}} \cdot \frac{I_{\gamma,reference}}{I_{\alpha',reference}}, \tag{38}$$

where:

X_γ = Mass fraction of γ-austenite

$X_{\alpha'}$ = Mass fraction of α'-martensite

RIR_γ = Reference Intensity Ratio for γ-austenite

$RIR_{\alpha'}$ = Reference Intensity Ratio for α'-martensite

$I_{\gamma,observed}$ = Observed intensity of γ-austenite

$I_{\gamma,reference}$ = Reference intensity of γ-austenite

$I_{\alpha',observed}$ = Observed intensity of α'-martensite

$I_{\alpha',reference}$ = Reference intensity of α'-martensite

Assuming that the only material phases present are α'-martensite and γ-austenite, the weight percentage of γ-austenite is determined by:

$$X_\gamma = \frac{100}{1 + \frac{X_{\alpha'}}{X_\gamma}} \tag{39}$$

Table 6 through Table 12 show the reference intensities of each peak, as well as the observed intensities of each peak. These reference values indicate the expected intensity order of the peaks. Note that some of the observed intensities are not in the same order as the expected values, which is another indication of preferred orientation being present in the samples. The location 2θ of each peak is also recorded. The mass intensities, shown in Tables 1b, 2b, and 3c, are calculated by comparing each observed peak of FCC-austenite to each observed peak of BCC-martensite. In a specimen with randomly oriented crystals, the comparison between each peak of FCC and each peak of BCC should result in the same calculated weight percentage of austenite. However, it can be seen that there is quite a bit of scatter depending on which peaks are compared. In particular, there is a relatively high prediction of austenite when comparing peaks with the 220-FCC peak. This indicates texture has an effect on these measurements.

Table 6: RIR values for analysis done on sample machined from original sheet material.

Face Centered Cubic	γ-austenite			
Reference Card:	PDF 03-065-4150			
RIR=	7.97			
hkl	Intensity (reference)	Intensity (observed)	2θ	Full Width at Half Maximum
111	100	13.9	43.753	0.256
200	42.5	9.1	50.889	0.412
220	17.8	51.5	74.781	0.383
311	16.6	17.1	90.726	0.63
222	4.6	1.2	96.005	0.617
400	2	0.8	118.342	0.57

Body Centered Cubic	α'-martensite			
Reference Card:	PDF 03-065-4899			
RIR=	10.77			
hkl	Intensity (reference)	Intensity (observed)	2θ	Full Width at Half Maximum
110	100	100	44.681	0.352
200	11.6	20.1	64.892	0.798
211	17.4	63.1	82.15	0.625
220	4.5	5.4	98.656	0.867
310	6.2	12.9	115.819	1.8

Table 7: Predicted weight percent of austenite for analysis done on specimen machined from original sheet material.

Peak Intensity Comparison		
hkl(γ):hkl(α')	Xα'/Xγ	Weight % austenite
111:110	5.32	15.81
111:200	9.22	9.78
111:211	19.31	4.92
111:220	6.39	13.53
111:310	11.08	8.28
200:110	3.46	22.44
200:200	5.99	14.31
200:211	12.53	7.39
200:220	4.15	19.43
200:310	7.19	12.21
220:110	0.26	79.63
220:200	0.44	69.29
220:211	0.93	51.88
220:220	0.31	76.52
220:310	0.53	65.27
311:110	0.72	58.19
311:200	1.24	44.55
311:211	2.61	27.74
311:220	0.86	53.70
311:310	1.49	40.09
222:110	2.84	26.06
222:200	4.92	16.91
222:211	10.29	8.86
222:220	3.40	22.71
222:310	5.90	14.49
400:110	1.85	35.09
400:200	3.21	23.78
400:211	6.71	12.97
400:220	2.22	31.06
400:310	3.85	20.62
	average austenite:	30
	average martensite	70

Table 8: RIR values for analysis done on specimen strained to 15.7% in the material rolling direction.

Face Centered Cubic	γ-austenite			
Reference Card:	PDF 03-065-4150			
RIR=	7.97			
hkl	Intensity (reference)	Intensity (observed)	2θ	Full Width at Half Maximum
111	100	4.9	43.695	0.326
200	42.5	3.5	50.794	0.66
220	17.8	22.4	74.739	0.622
311	16.6	4.3	90.629	0.976
222	4.6	0.3	95.98	0.676
400	2	0.5	118.868	0.359

Body Centered Cubic	α'-martensite			
Reference Card:	PDF 03-065-4899			
RIR=	10.77			
hkl	Intensity (reference)	Intensity (observed)	2θ	Full Width at Half Maximum
110	100	88.6	44.652	0.356
200	11.6	34.1	64.817	0.852
211	17.4	100	82.095	0.68
220	4.5	5.9	98.711	0.926
310	6.2	21.4	115.833	1.987

Table 9: Predicted weight percent of austenite for analysis done on specimen strained to 15.7% in the material rolling direction.

Peak Intensity Comparison		
hkl(γ):hkl(α')	Xα'/Xγ	Weight % austenite
111:110	13.38	6.95
111:200	44.40	2.20
111:211	86.80	1.14
111:220	19.80	4.81
111:310	52.13	1.88
200:110	7.96	11.16
200:200	26.42	3.65
200:211	51.64	1.90
200:220	11.78	7.82
200:310	31.02	3.12
220:110	0.52	65.75
220:200	1.73	36.65
220:211	3.38	22.83
220:220	0.77	56.47
220:310	2.03	33.01
311:110	2.53	28.32
311:200	8.40	10.64
311:211	16.42	5.74
311:220	3.75	21.07
311:310	9.86	9.21
222:110	10.05	9.05
222:200	33.36	2.91
222:211	65.21	1.51
222:220	14.88	6.30
222:310	39.17	2.49
400:110	2.62	27.60
400:200	8.70	10.31
400:211	17.01	5.55
400:220	3.88	20.49
400:310	10.22	8.92
	average austenite:	14
	average martensite:	86

Table 10: RIR values for analysis done on specimen strained to 15.9% in the material cross direction.

Face Centered Cubic	γ-austenite			
Reference Card:	PDF 03-065-4150			
RIR=	7.97			
hkl	Intensity (reference)	Intensity (observed)	2θ	Full Width at Half Maximum
111	100	6.5	43.723	0.324
200	42.5	3.6	50.817	0.685
220	17.8	29.4	74.794	0.639
311	16.6	5.5	90.654	0.973
222	4.6	0.5	96.308	0.224
400	2	0		
Body Centered Cubic	α'-martensite			
Reference Card:	PDF 03-065-4899			
RIR=	10.77			
hkl	Intensity (reference)	Intensity (observed)	2θ	Full Width at Half Maximum
110	100	100	44.68	0.366
200	11.6	47.1	64.828	0.873
211	17.4	85	82.157	0.694
220	4.5	7.2	98.706	0.988
310	6.2	30.1	115.79	1.969

Table 11: Predicted weight percent of austenite for analysis done on specimen strained to 15.9% in the material cross direction.

Peak Intensity Comparison		
hkl(γ):hkl(α')	Xα'/Xγ	Weight % austenite
111:110	11.38	8.07
111:200	46.23	2.12
111:211	55.62	1.77
111:220	18.22	5.20
111:310	55.27	1.78
200:110	8.74	10.27
200:200	35.47	2.74
200:211	42.68	2.29
200:220	13.98	6.68
200:310	42.41	2.30
220:110	0.45	69.06
220:200	1.82	35.47
220:211	2.19	31.36
220:220	0.72	58.25
220:310	2.18	31.49
311:110	2.23	30.93
311:200	9.07	9.93
311:211	10.91	8.40
311:220	3.57	21.86
311:310	10.84	8.44
222:110	6.81	12.81
222:200	27.64	3.49
222:211	33.26	2.92
222:220	10.89	8.41
222:310	33.05	2.94
	average austenite:	15
	average martensite:	85

Table 12: Average values from RIR analyses.

Specimen	Average Weight % Austenite	Average Weight % Martensite
Original	30	70
Rolling	14	86
Cross	15	85

4.1.4.2 Analysis Method 2: Whole Pattern Fitting Method

The second method used to analyze the results is performed as an effort to circumvent incorrect measurements due to texture effects. This method of whole pattern fitting (WPF) involves modeling the texture of the specimens in order to fit the entire X-ray diffraction pattern obtained. The computer software Jade is used to perform the whole pattern fitting procedure. The key steps involved in performing this data analysis are:

1. Provide Jade with the chemical composition and crystal structure of the material being analyzed. This allows Jade to determine the location (2θ) of the peaks it expects to see in the X-ray diffraction scan data. The chemical composition provided to Jade for this analysis is: 75% iron, 18% chromium, and 7% nickel.
2. Allow Jade to fit the background noise and all of the peaks with no texture involved.
3. Identify possible preferred orientations by noting large differences in the expected diffraction pattern and the observed peaks (i.e., if a peak is much higher than the data cards suggest it should be in relation to the maximum intensity peak, this peak could indicate a possible preferred orientation). At least one peak in each of the scans has an intensity that is much different than is predicted for a completely random configuration of the chemical composition provided to Jade. Therefore, in each case, the peak that showed the most noticeable difference was established and its slip plane normal is identified as a preferred orientation in the specimen being examined.
4. Again, allow Jade to fit the data, this time including texture effects.
5. Jade outputs the weight percentage of FCC-austenite and BCC-martensite it expects to have produced the diffraction pattern. Therefore, from the material composition and the identified preferred direction, Jade fits the diffraction data and determines the percent of the FCC-austenite and BCC-martensite which would produce such a diffraction pattern.

Several iterations are involved in each of the above steps in order to accurately fit the data and model the texture. The resulting predicted weight percents of austenite and martensite for each of the three specimens are shown in Table 13.

Table 13: Data from Whole Pattern Fitting Analyses (all deemed to be within ~ +/- 2%).

Specimen	Average Weight % Austenite	Average Weight % Martensite
Original	33	67
Rolling	11	89
Cross	14	86

4.1.5 Conclusions of X-Ray Diffraction Study

Table 13 shows that there is martensite present in all three specimens analyzed. It can also be concluded that while there is martensite present in the original material, there is an increase in the relative mass of martensite versus austenite after the specimens have been deformed. The RIR analyses and the WPF analyses provide the same general trend of weight percent austenite versus weight percent martensite. This is encouraging because these are different methods for analyzing the data first by including no texture correction and second by trying to account for texture effects. Because the WPF method involves modeling the actual texture, it is deemed to be the more reliable approach. Therefore, after performing whole pattern fitting on the three specimens, this X-ray diffraction study indicates that the weight percent of retained austenite is about 33% in the original material, 11% in the specimen strained in the material rolling direction, and 14% in the specimen strained in the material cross direction.

The drawbacks to this method are in the number of uncertainties or possible sources of error as well as the fact that this method requires interrupted tests. In addition, it is an extremely time-consuming task because each measurement takes several hours to run, and the analysis afterwards requires significant knowledge of X-ray diffraction.[1] One of the main sources of error is that accurate results from X-ray diffraction analysis require texture-free specimens. Even when using the WPF method to fit the texture, the texture effects may not be completely eliminated. Another issue with this method is the shallow penetration depth of the X-ray beams. Because the depth of penetration in this study is between 4 μm and 13 μm, the surface and only a shallow portion near the surface of the

[1] The help of Dr. Scott Speakman is gratefully acknowledged in performing both the measurements and the subsequent analysis.

material is investigated. The surface properties may not be completely representative of the bulk properties. Specifically, if the martensite transformation is at all susceptible to surface defects or edge effects, the martensite content at the surface may not be representative of the center of the gauge section of the specimen, and the measurements could be misleading.

Therefore, from this study, the following two conclusions can be made:

1 – There is indeed a significant transition from FCC-austenite to BCC-martensite when the material is subjected to large deformations at room temperature.

2 – It can be reasonably concluded that when the material is strained in the rolling direction, more of the austenite is transferred to BCC-martensite than if the material is strained in the cross direction.

4.2 Magnetic Induction Method Using Feritscope

Employing the magnetic induction method for measuring the martensite content is done in-situ by using a Fischer Feritscope MP30E, shown in Figure 14. The concept behind this technique involves determining the martensite content by measuring the magnetic permeability of the specimen. The output of the device is Ferrite Number (FN), based on the specifications of ISO-8249, which describes quantitative calibration of the magnetic field. The method described in this standard involves relating the tear-off force required to pull a magnet off a magnetic material to the FN. The FN is proportional to the magnetic permeability of the specimen. The Feritscope used in this study is originally designed for measuring δ-ferrite content of steels. Its measurement range is between 0% and 100% δ-ferrite, which corresponds to an FN between 0 and 125. The calibration between %δ-ferrite and FN provided by the manufacturer is given in Figure 15. This curve gives the following conversion from FN to % ferrite:

$$\%Fe = 7 \cdot 10^{5} FN^{3} - 0.0144 FN^{2} + 1.422 FN - 1.41 \tag{40}$$

While the device is intended for determining δ-ferrite content, due to the fact that martensite is also a magnetic phase, this device can be used to determine the amount of

martensite. However, it must be carefully calibrated in order to produce quantitative results. Any evolution of the FN is attributed to martensite evolution because it is the magnetic phase in this steel which evolves during straining.

The Feritscope includes a control and display unit, a hand-held probe, and the ability to transfer data to a computer for analysis. To take a measurement, the probe is held in contact with the specimen surface. In the probe, there is a soft iron core, with two coils surrounding this core. The Feritscope sends a low frequency alternating current through the input coil, which in turn generates a magnetic alternating field that penetrates into the specimen. The permeability of the specimen and its magnetic properties alter the field and induce an alternating voltage in the detection coil. This voltage is transmitted back to the Feritscope display unit, and is proportional to the δ-ferrite content in the volume measured. In the absence of δ-ferrite in the volume, this voltage is proportional to the martensite content in the volume because the voltage is a measure of the magnetic permeability. This is an attractive method for measuring martensite because it allows for in-situ measurements of the martensite evolution, but it requires very careful calibration.

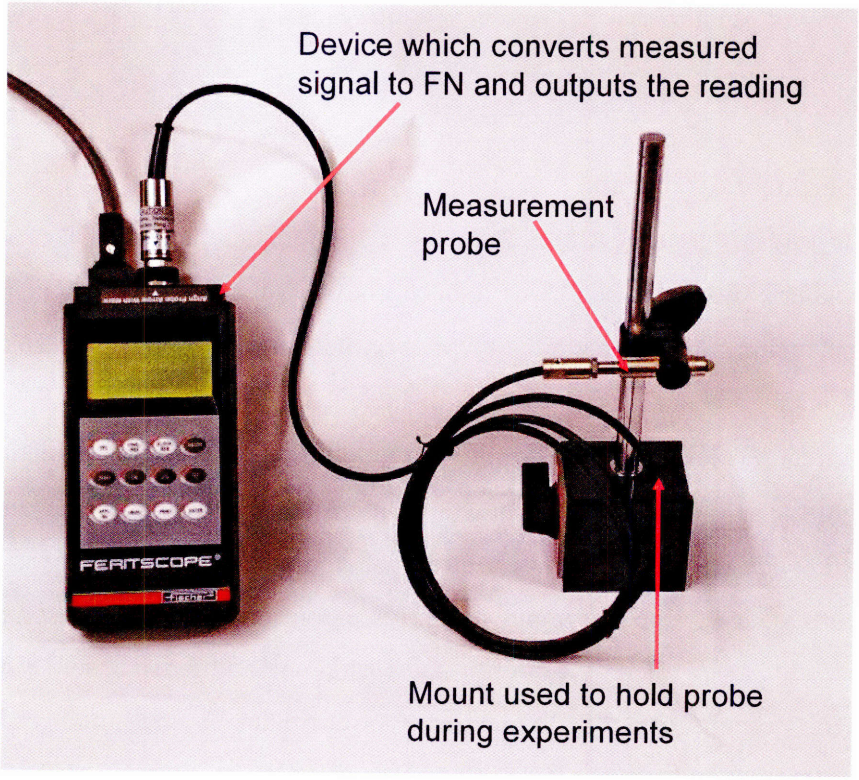

Figure 14: Fischer Feritscope MP30E.

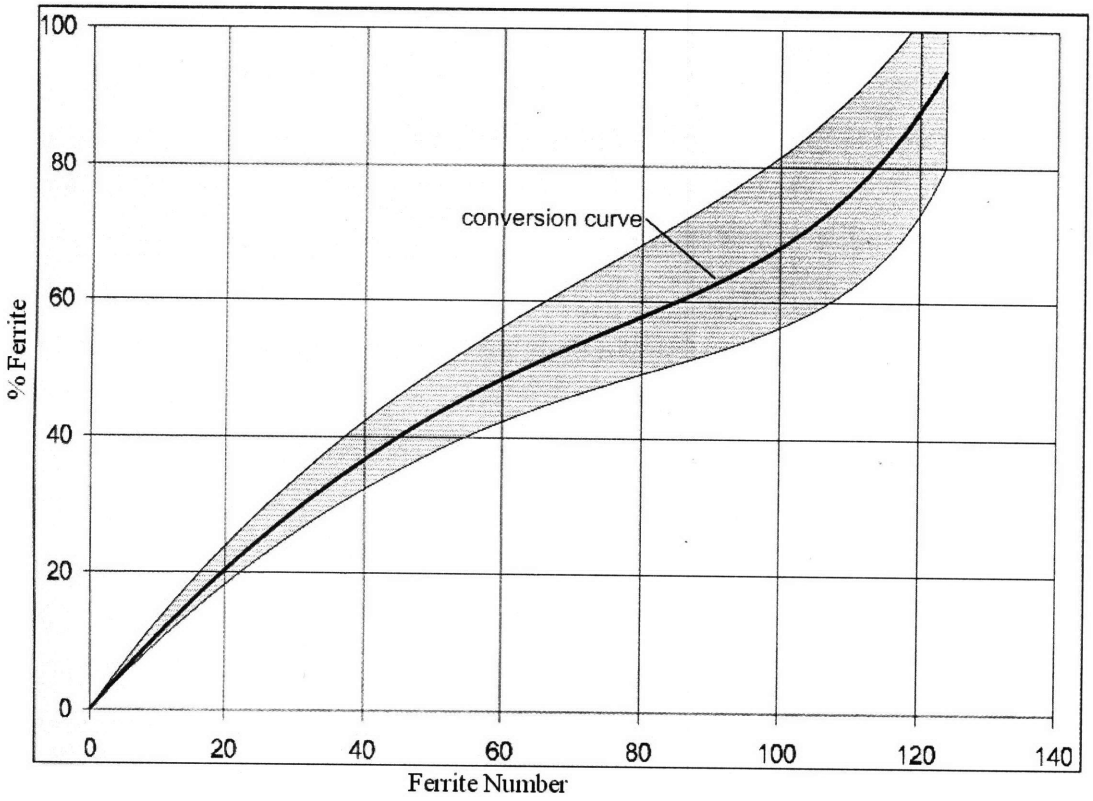

Figure 15: Calibration curve between Ferrite Number and % δ-ferrite provided by Fischer (from Feritscope MP30E-S Operator's Manual).

4.2.1 Experimental Program

The testing program for measuring the evolution of martensite as a function of strain and material direction begins with machining the uniaxial tension specimens using a water jet machine. The geometry of these specimens is shown in Figure 16. A total of twelve specimens are machined - four with their tensile axis aligned with each of the following directions: the material rolling direction, the cross-rolling direction, and 45 degrees from the rolling direction. These specimens are then loaded under displacement control at 0.5 *mm/minute* to a plastic strain of about 15%, 10%, or 5%. Once the specimens are loaded to the maximum strain, force-controlled loading is used to decrease the tensile load to 0 *kN*, thereby capturing the elastic unloading response. While each of the specimens is being loaded and unloaded, four attributes are measured recorded: FN, displacement, force, and temperature. The FN is recorded at intervals of 0.8 seconds by

placing the probe in contact with the gauge section of the specimen and putting the Feritscope in "continuous reading" mode. The other three measurements are taken at a rate of either 1 *Hz* of 0.5 *Hz*. The vertical force is measured by two 100 *N* load cells and directly input into the DIC software. Temperature is monitored using a K-type thermocouple that is taped to the specimen gauge section. The voltage measured by the thermocouple is input into an Omega programmable digital thermocouple controller which converts the signal to temperature. The temperature is then converted to a voltage corresponding to a calibration curve defined by the user, and this output voltage is transmitted to the DIC software. Displacement is measured by the optical method described previously. For these tests, the pixel edge length is about 40 μm. The experimental setup is shown in Figure 17 and Figure 18.

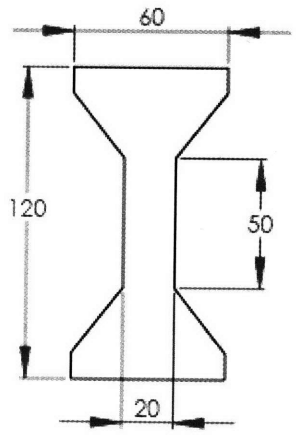

Figure 16: Geometry of uniaxial tension specimens used in Feritscope and micrography studies (dimensions in *mm*; thickness is 1.5 *mm*).

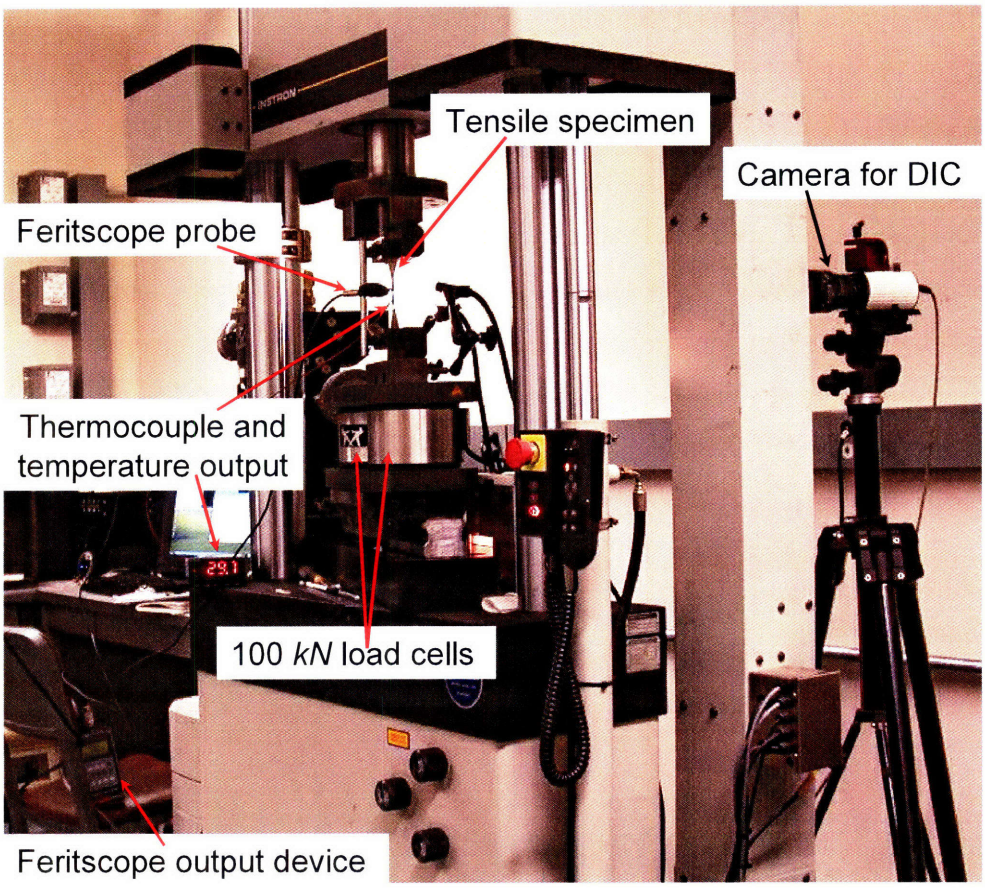

Figure 17: Experimental setup for uniaxial tension, monitoring force, displacement, temperature, and Ferrite Number.

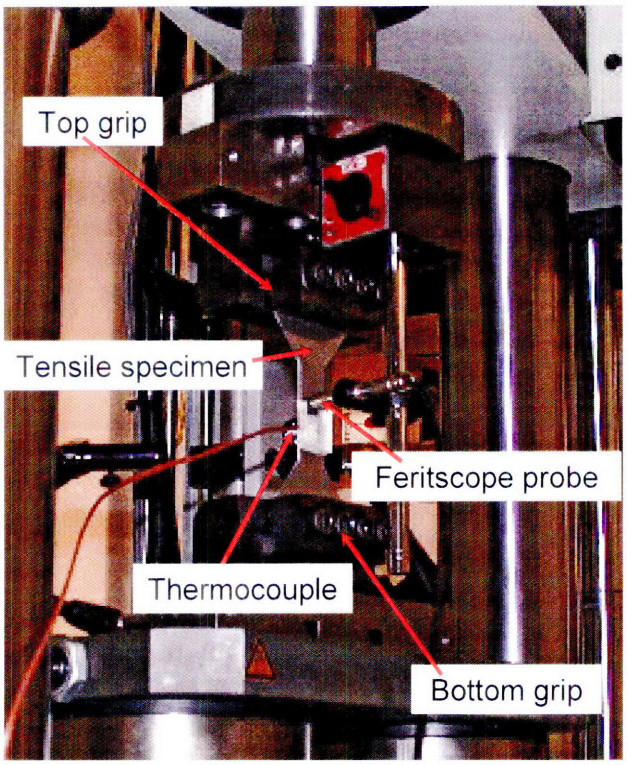

Figure 18: Close view of test setup highlighting Feritscope and thermocouple placement.

During these tests, it was noted that the FN measurement value is extremely sensitive to the distance between the probe tip and the specimen surface. Therefore, an effort is made to ensure the probe tip is always in contact with the specimen. However, small drops in FN most likely indicate a slight separation between the probe tip and the specimen surface.

4.2.2 Results

The true stress-strain curves developed provide extremely repeatable results. In addition, the FN versus strain demonstrates repeatability of the FN measurement. In order to illustrate the evolution of FN with the stress and strain state, the FN is scaled by 25 and plotted with the true stress and strain as shown in Figure 19. There are several interesting features of the FN evolution. First, the FN decreases during the initial loading period in the elastic region and begins to increase as the nonlinear yielding behavior begins. Second, the FN increases approximately linearly with increasing strain while loading during strain hardening. Third, there is a dramatic increase in FN during the

elastic unloading period. Finally, the fact that the tests are quite repeatable is a good indication that this in-situ measurement technique is a viable method for capturing the real-time martensite evolution.

These tests are performed with specimens with their tensile axes aligned with the material cross-rolling direction and 45 degrees from the rolling direction. Similar repeatability is observed, and the results are shown in Figure 20 and Figure 21. It is important to note that the four specimens tested in the rolling direction and the four specimens tested in the cross-rolling direction were all cut from the same stainless steel 301LN sheet, while the four specimens tested in the 45-degree direction were cut from a second sheet. This accounts for the initial discrepancy in FN measured.

The measurement of temperature is less revealing. In each of the tests, there is an initial temperature rise in the gauge section of the tensile specimens from room temperature to about $30^{o}C$. However, this temperature reaches a plateau during the plastic flow portion of the test. A typical plot of temperature versus logarithmic strain is shown in Figure 22. Because the tests are performed at a quasi-static strain rate, heat is able to exit the specimen. Therefore, the fact that the specimens do not show an increase in temperature with strain rate is consistent with the predictions. It is noted that in each of the tests, the temperature is always between $-60^{o}C$ and $83^{o}C$, which is the range found by Santacreau et al. (2006) in which this stainless steel 301LN exhibits phase transformation.

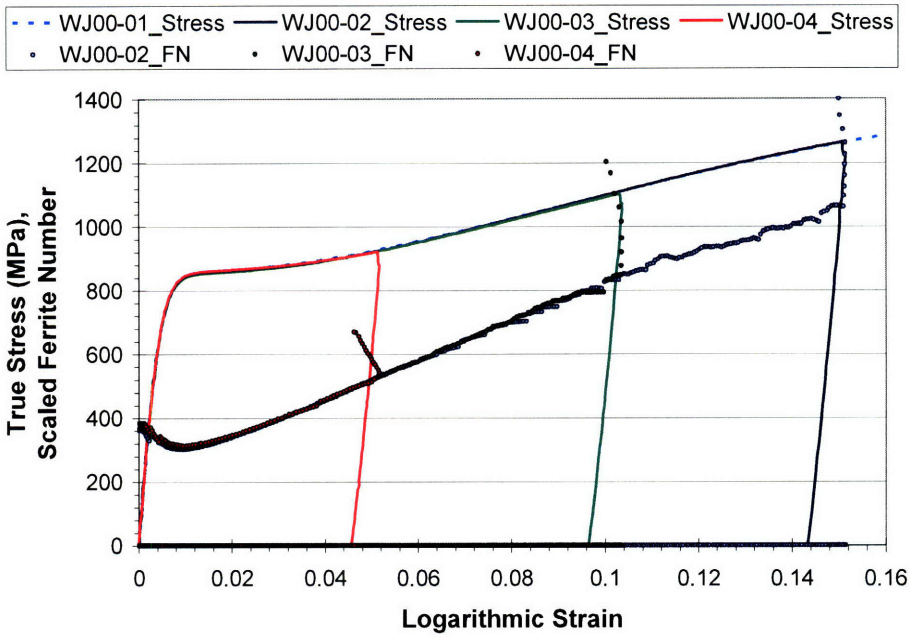

Figure 19: True stress and scaled Ferrite Number versus logarithmic strain for specimens strained 5%, 10%, and 15% in the material rolling direction.

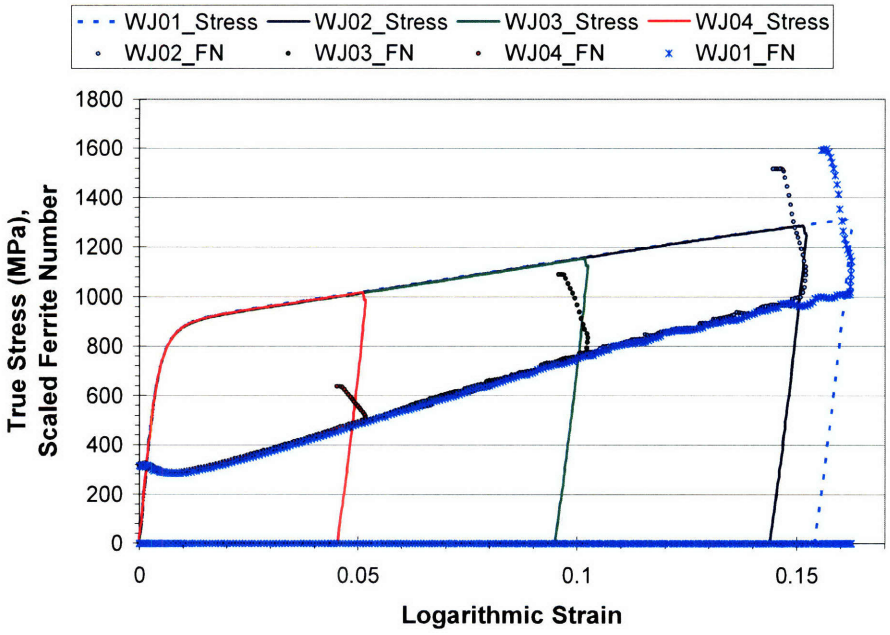

Figure 20: True stress and scaled Ferrite Number versus logarithmic strain for specimens strained 5%, 10%, and 15% in the material cross-rolling direction.

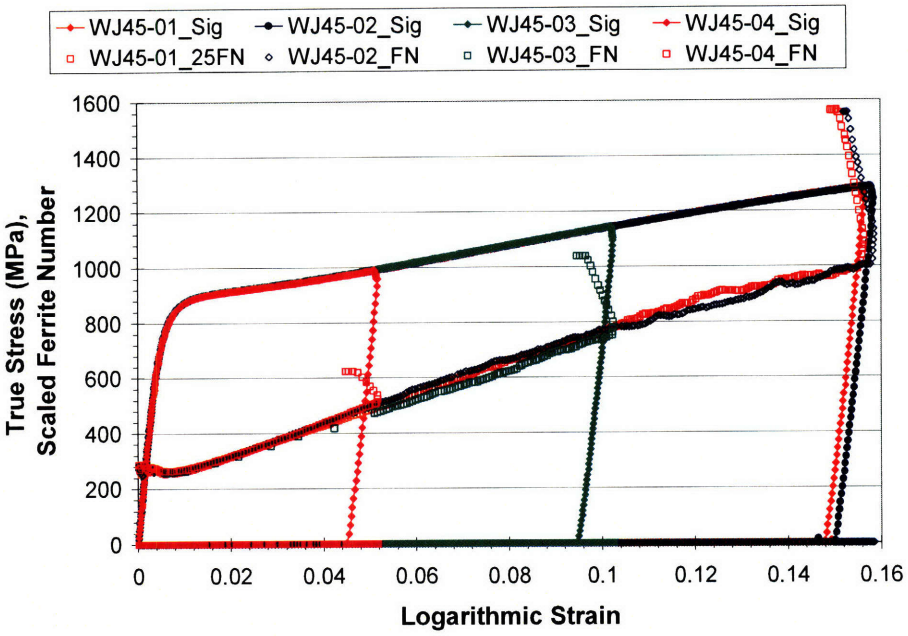

Figure 21: True stress and scaled Ferrite Number versus logarithmic strain for specimens strained 5%, 10%, and 15% 45 degrees from the material rolling direction.

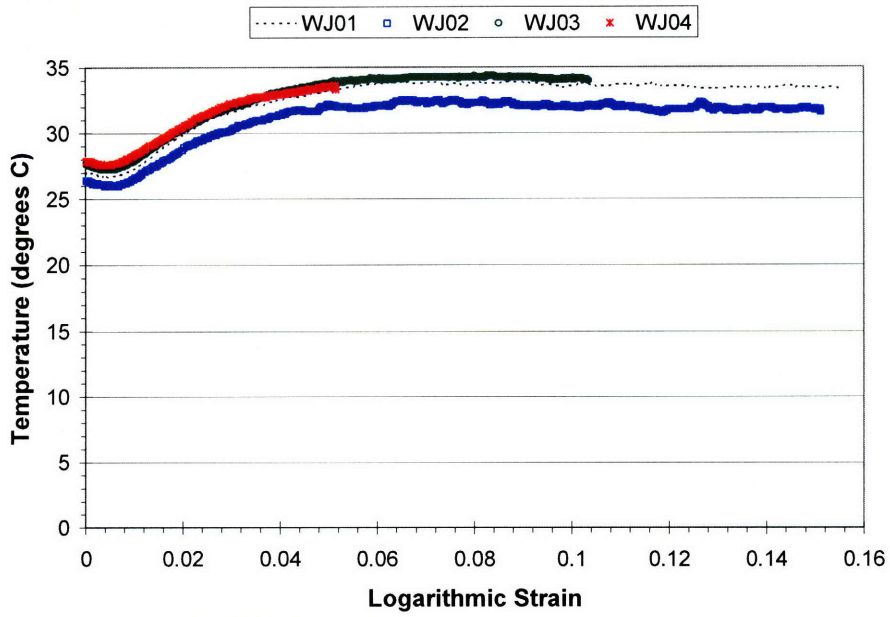

Figure 22: Temperature versus logarithmic strain for specimens strained 5%, 10%, and 15% in the material rolling direction.

4.2.3 Analysis

Before complete quantitative values are assigned to the martensite content in terms of FN, important observations can still be drawn. Because FN is a measure of the material magnetic permeability, as the martensite increases and therefore the magnetic composition of the material increases, the trend of increasing FN does indeed indicate an increase in martensite content. In each of the three directions, the FN increases slightly and then decreases in the elastic loading region of the stress strain curve, and then increases relatively linearly during plastic yielding and strain hardening. During the elastic unloading, the FN increases significantly.

Comparisons can be made between the FN in each of the three material directions studied. Consistent with the X-ray diffraction conclusions, the martensite content is higher when the material is strained in the material rolling direction than in the cross direction. The evolution of the FN in the specimens strained in the material direction 45 degrees from the rolling direction seems to more closely follow the behavior of the cross-rolled direction. For the majority of the plastic flow region, the FN is slightly higher in the 45-degree direction than in the 90-degree direction, and lower than that of the 0-degree direction. The ultimate FN values after elastic unloading indicate that in the unloaded condition, the material strained in the 0-direction has the most martensite, and the material strained in the 90-degree direction has the least, with the final martensite content in the 45-degree direction in between that in the rolling and cross-rolling directions. Note that the plastic strain in each specimen is not exactly the same, and the final plastic strain values of each specimen are shown in Table 14. Figure 23 gives a plot of these results. This shows that of the three material orientations tested, the measured FN is highest when the material is strained in the material rolling direction, regardless of the level of strain. The specimens strained in the cross-rolling direction and 45 degrees from the rolling direction follow each other more closely, but the FN in specimens strained in the 45 degree direction is always slightly below that in specimens strained in the cross-rolling direction. In addition, the difference in FN between specimens strained in the rolling direction and those strained in the cross-rolling direction increases with increasing strain.

Table 14: Plastic strain induced and the final value of Ferrite Number in each of the uniaxial tension specimens.

Degrees from rolling direction	Specimen	Percent Plastic Strain	Ferrite Number
00	01	15.2	69
	02	14.5	66
	03	9.8	48
	04	4.7	27
90	01	15.6	64
	02	14.6	61
	03	9.7	44
	04	4.7	26
45	01	15.0	62
	02	15.1	62
	03	9.7	41
	04	4.7	25

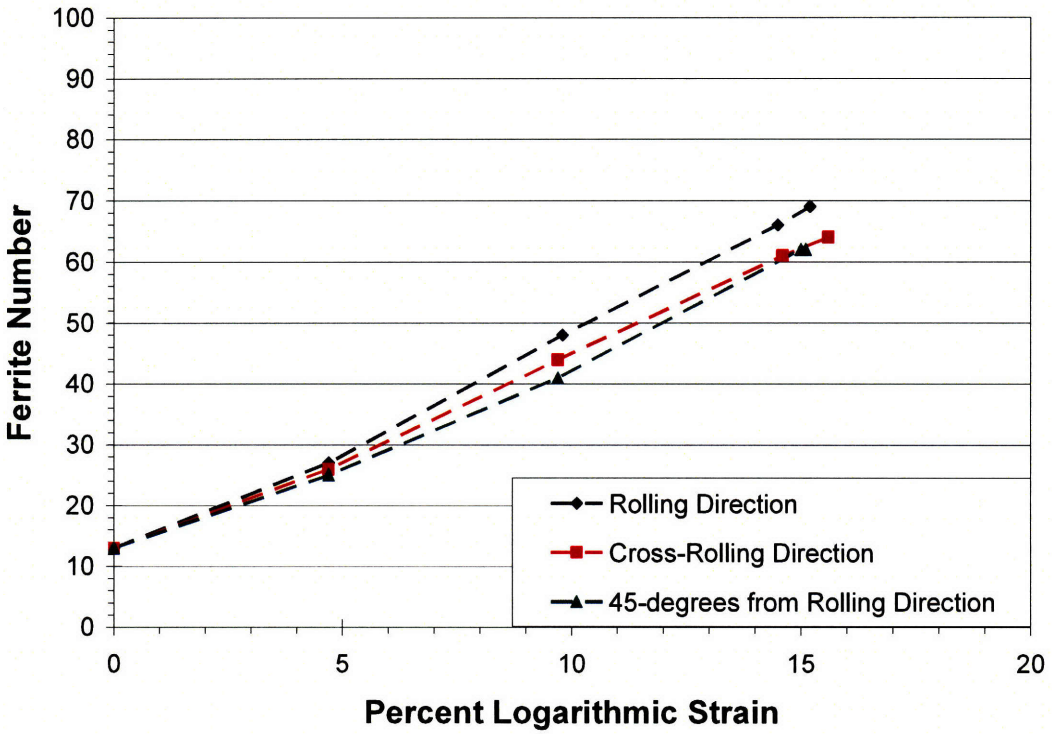

Figure 23: Final Ferrite Number versus total strain in three material directions.

4.2.4 Conclusion of measurements using Feritscope

The Feritscope is a powerful method for testing because it allows for in-situ measurements of martensite content. This allows for continuous data during tests in order to relate direction, strain, and stress state to the martensite evolution. Although use of the Feritscope seems to be the ideal method for measuring martensite, this method does have some disadvantages. The major issue with this method is that the output of the Feritscope is either FN or % δ-ferrite. Therefore, the output is calibrated for measuring a different phase than the one of interest in this thesis. However, this study confirms that the martensite evolution does indeed cause an evolution of the FN measurement, indicating that it is possible to relate the martensite content to the measured FN. Therefore, the Feritscope must be calibrated by relying on another measurement technique to determine the correlation between FN and martensite content, and subsequently the martensite evolution as a function of direction, stress state, and strain.

4.3 Micrography

The final method used to measure martensite content is through micrography. This approach allows one to highlight the desired features in the microstructure via polishing and etching, and these features can then be examined through a microscope. The main steps for preparing a specimen for a micrograph, as defined by Volume 8 of the ASM Metals Handbook, are: sectioning, mounting, grinding, polishing, and etching.

4.3.1 Preparation of the Specimens for Micrography

The specimens used in this study are extracted from the gauge sections of the uniaxial tension specimens strained along the rolling direction. Sections are cut from the specimens, which, as discussed in the previous section, have been subjected to 15%, 10%, and 5% plastic strain in the material rolling direction. Sections are also cut from the original cold-rolled sheet material. The microstructure of each of these specimens is examined after adequate preparation to determine the area percentage of martensite present in each as well as the spatial distribution of the martensite.

4.3.1.1 Sectioning

First the specimens are cut from the plastically deformed gauge sections using a water jet machine. Each gauge section is cut into seven smaller sections. A diagram showing how the gauge section is divided is given in Figure 24. Four of the sections have approximate dimensions of 10 *mm* by 20 *mm*. The remaining three specimens have dimensions of approximately 10 *mm* by 6 *mm*, and they are stacked and bonded together for subsequent mounting and polishing procedures. The purpose of the stacking and bonding is to obtain through-thickness information of the martensite spatial distribution and shape.

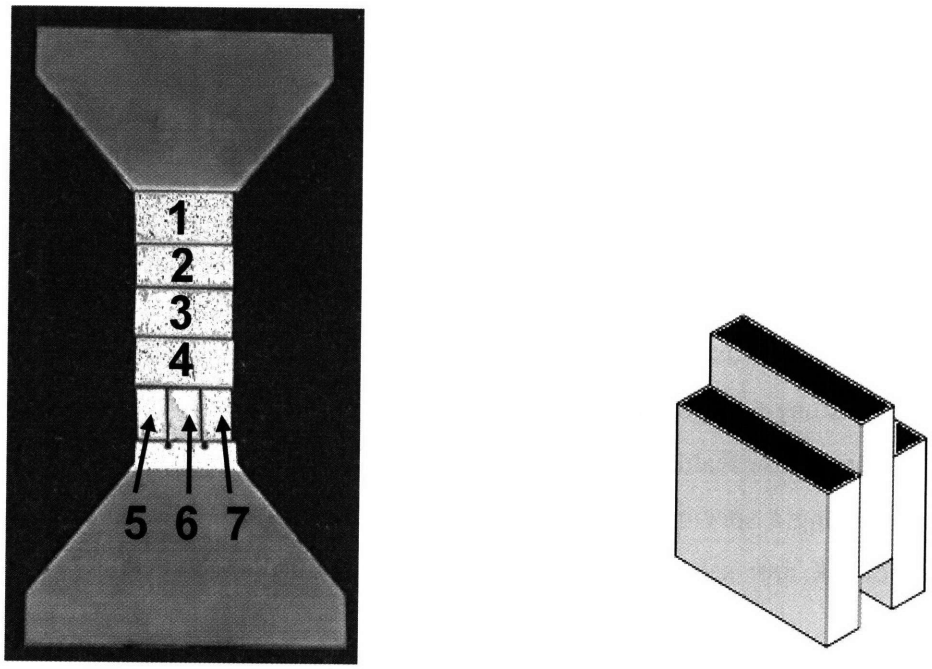

(a) (b)

Figure 24: Sectioned uniaxial dog bone specimen which has been strained to a plastic strain of approximately 5% in the rolling direction. Each of these sections is referred to with a name beginning with that of the large specimen (e.g., WJ004) and ending with a number 1 through 7 as shown in (a). Sections 5, 6, and 7, are stacked and bonded as shown in (b) with the black representing the width of the gauge section, the gray representing the tensile plane of the large specimen, and the white representing the surface to be polished.

4.3.1.2 Mounting

Mounting is the next step, and is performed to provide for adequate handling of the specimens for grinding and polishing. The specimens are mounted in Buehler's Konductomet, which is comprised of graphite, fibrous glass, hexamethylenetetramine, phenol, and silicon dioxide. Figure 25 shows the mounting press used. Each specimen is placed on the mounting platen, and the platen is lowered. A scoop of Buehler's Konductomet, is poured into the vertical cavity. A cap is inserted in the top of the cavity, and the machine begins the mounting process. In order to embed the specimen in the mount, the mounting powder and specimen are subjected to 4200*psi* (30*MPa*) at 150^{o}C. This pressure exerts a maximum of only 3% of the final flow strength of these specimens (minimum final final flow strength is 912*MPa*), and therefore it is deemed that this mounting does not alter the microstructure. A typical mounted specimen and a specimen used to study through-thickness features are shown in Figure 26.

Figure 25: Buehler mounting press used to mount specimens.

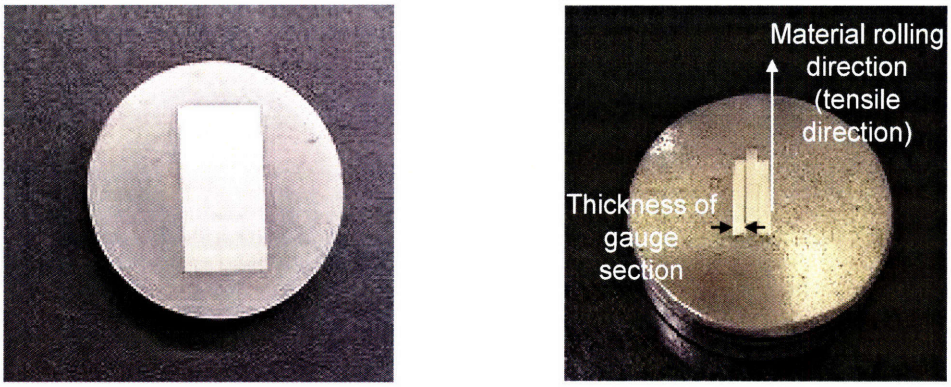

(a) (b)

Figure 26: Sample specimens mounted in 1.25*in* diameter Konductomet. A typical specimen, whose tensile axis is examined is given in (a), and (b) shows sections 5, 6, and 6, after stacking and bonding, allowing for examination of the through-thickness features.

4.3.1.3 Mechanical Grinding and Polishing

The next step is mechanical grinding and polishing of the mounted specimens. Grinding and polishing are done to create a very flat plane that can be examined in a microscope. These processes incur a shallow level of plastic deformation at the surface of the specimen because grinding essentially tears off the top surface of the specimen to even out the surface. A Buhler automatic polishing machine, shown in Figure 27, is used to produce even polishing and to apply the exact same procedure to each of the samples. The grinding is performed using silicon carbide abrasive films, beginning with 500 grit (30 μm), then using 1200 grit (14 μm) and finally using 4000 grit (5 μm). During each of the grinding steps, a force of 25N is applied to each of the samples to assist the grinding and to hold the specimens in place. Grinding is done at 300 *rpm*, with the specimens rotating counterclockwise while the wheel spins clockwise. Water is used to constantly clean the grinding paper and remove inclusions which could damage the surface of the specimens. Each grinding paper is used for four total minutes of grinding to ensure that the grooves incurred from the previous grinding paper are removed. The polishing is performed using a polishing cloth adhered to the lapping wheel with a 0.3 μm aluminum oxide suspension spread over the wheel. A pressure of 25 N is applied to the samples, and a polishing speed of 150 *rpm* is used with both the samples and the lapping wheel

spinning in the same direction. A total of four minutes of polishing is performed on each of the specimens, and after each minute, the specimens and the polishing wheel are cleaned thoroughly with distilled water to remove any potentially damaging abrasions.

Figure 27: Buehler automatic polishing machine used in grinding and polishing procedures.

4.3.1.4 Etching

The final step in preparing the specimens for micrography is etching. Beraha's tint is used for etching this austenitic stainless steel to reveal martensite. Beraha's tint is comprised of 50 *ml* water, 10 *ml* hydrochloric acid (HCl), and 0.15 *g* potassium metabisulfite ($K_2S_2O_5$). This etchant is applied for 15 seconds by immersing the specimen in the etchant and agitating the specimen to ensure that the surface is

continuously in contact with new etchant. After the 15 seconds of etching, the specimen is cleaned in water and then alcohol.

The etchant preferentially attacks certain grains based on their crystal structure, thereby dissolving the surface of different phases of the metal faster than others. This results in the exposed portion of some grains to be in a plane not parallel to the initially polished plane. Therefore, there is a difference in outward normal between the un-etched portions of the specimen and the etched regions. The different orientations of the grains on the surface reflect light at angles different from the polished plane. Therefore, when the illuminated specimens are observed in the microscope, grains aligned with the polished plane appear light, while grains that have been partially dissolved will reflect the light at a different angle and therefore appear dark. This is how the phases are differentiated.

4.3.2 Analyzing Micrographs

Micrographs are created by taking digital images of the etched specimens through an optical microscope. The microscope used in this study is a Zeiss Axioplan Optical Microscope into which a computer-controlled digital camera is integrated. Using AxioVision, the image from the microscope is transmitted to the computer screen, and a digital micrograph can be captured. The magnification used for the micrographs is 10x, 20x, 50x or 100x. Each micrograph is made such that the material rolling direction is vertical, except those made from the specimen cut from the original cold rolled sheet in which the cross-rolling direction is vertical.

After the micrograph is created, it is then filtered using Matlab's image processing toolbox. In order to get a high quality micrograph that can be used for quantitative analysis, the image is first converted to grayscale, and then a filter is used to increase the contrast between light and dark areas. The resulting image is stored as a two-dimensional matrix in Matlab where each pixel location has an intensity value from 0 to 255. An intensity of 0 corresponds to a black pixel while an intensity of 255 corresponds to a white pixel. It has been determined that the martensite is seen in the micrograph by dark lines as well as dark smooth areas. The light areas correspond to austenite. This identification of the phases present is shown in Figure 28.

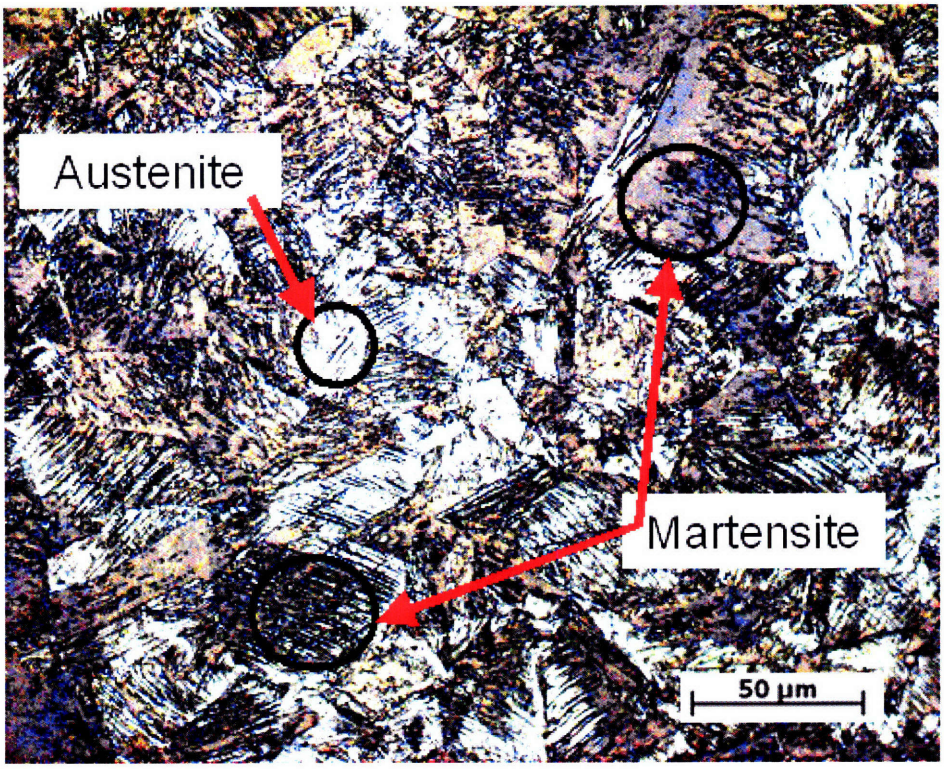

Figure 28: Identification of austenite and martensite regions in a sample micrograph.

Initial analysis is performed by converting each grayscale image to a binary black and white image. However, these calculations result in a significant amount of scatter. This scatter can be attributed to the fact that when converting the image to grayscale and then to black and white, there is a dependence on the microscope illumination used. This is because Matlab's threshold for differentiating light and dark pixels remains the same (pixels with intensities between 0 and 128 become black and those with intensities from 129 to 255 become white), while the micrograph as a whole is lighter or darker depending on the microscope parameters in use. Therefore, if more reflected light is used, the micrograph will be lighter, and result in a lower calculation of martensite than if less reflected light is used, and the micrograph as a whole is darker. This dependence on microscope parameters on resulting area calculations is illustrated in Figure 30, where the same image is taken with different levels of reflected light. The light was varied from 70%, to 75%, to 80% of the available reflected light supplied to the microscope, and this

resulted in a calculated amount of martensite of 61%, 63%, and 58%, respectively, using Matlab's predefined constant threshold value to differentiate white from black.

Another variable which can cause measurement scatter is the etching procedure. A longer etch time creates deeper grooves or may begin to etch the austenite as well as the martensite. This results in more grains that are not parallel to the polishing plane, and therefore an overall darker appearance of the sample when viewed through the optical microscope. Each sample in this study was submerged with agitation for roughly 15 seconds, but any variation of that time may cause visible differences when the specimen is viewed in the microscope. In addition, differences in the agitation may cause slight differences in etching effectiveness, and the same end result as different etching times.

To eliminate the dependence on microscope illumination and slight alterations in etching procedure, more careful analysis is required. First, each micrograph is read into Matlab and converted to grayscale. An example of this is shown in Figure 29 where the image in Figure 28 has been converted to gray scale. Then the image is examined to visually determine which regions of pixels correspond to martensite. The intensity values of pixels in the lightest areas that correspond to martensite are manually probed, and the highest intensity value of the martensite in the image is determined. This intensity is then deemed to be the threshold for differentiating light from dark pixels. A Matlab code is then used to scan the entire matrix of pixel intensity values to calculate the number of pixels below the threshold value which correspond to the martensite area percentage. To demonstrate that this method can greatly reduce the dependence of the measurement on microscope reflected light, this method is used to determine the area percentage of martensite in the three micrographs in Figure 30 which differ only by the intensity of the reflected light used to create each micrograph. The area composition of martensite is calculated to be 89% in each of these micrographs when adjusting the threshold to differentiate austenite and martensite to an intensity of: 207 for the micrograph in (a), 215 for the micrograph in (b), and 214 for the micrograph in (c). Although this method is very delicate and may include some user error, it does have the desired ability to eliminate the calculation dependence on illumination and etching procedure.

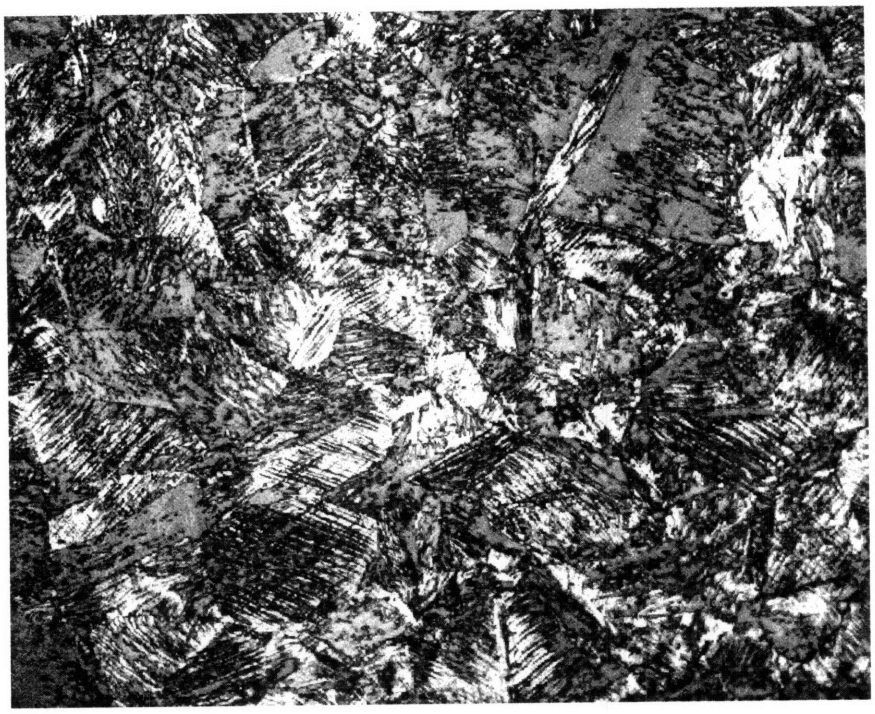

Figure 29: Micrograph in Figure 28 converted to a gray scale image.

Several micrographs were made of the original specimens and those subjected to 5%, 10%, or 15% strain in the material rolling direction. Some of the resulting micrographs are given in Figure 31 through Figure 34. As mentioned above, each micrograph is converted to a grayscale image, the contrast is increased. The method described above is then used to determine the lightest intensity value of martensite and then the percentage of martensite is calculated by adjusting the threshold to differentiate martensite from austenite accordingly. While several micrographs were taken at 10x, 20x, 50x, and 100x, the micrographs at 50x were the most clear while still fitting several typical grains inside each image. Micrographs taken at 10x or 20x were not very clear, and micrographs taken at 100x gave images on the order of the length scale of a grain, and therefore, this data was used for inspection of martensite structure rather than quantitative analysis. Therefore, all precise measurements for calibration were taken from micrographs with a magnification of 50x. The results of this study are given in Table 15, which compares the measured martensite area with the FN and the % δ-ferrite measured by the Feritscope. These results show qualitatively that the measurements of

martensite via micrography and Feritscope are consistent with each other. Figure 36 shows the martensite content calculated with micrographs versus the FN or %Fe output from the Feritscope. The preliminary calibration curve between output FN and martensite percentage is given by:

$$\%Martensite = 0.59 \cdot (FN) + 57 \tag{41}$$

The preliminary calibration curve relating output %Fe and martensite percentage is given by:

$$\%Martensite = 0.92 \cdot (\%Fe) + 49 \tag{42}$$

Micrographs are also made of through-thickness samples for specimens strained in the rolling direction. Figure 36 shows a micrograph with a magnification of 20x of a specimen which has been strained 5% in the material rolling direction. The micrographs made in the through-thickness direction show what appear to be elongated grains, as well as possible cracks, in the vertical direction. These features are assumed to be artifacts from the cold-rolling process to fabricate the sheets, which are subsequently amplified through straining in the material rolling direction.

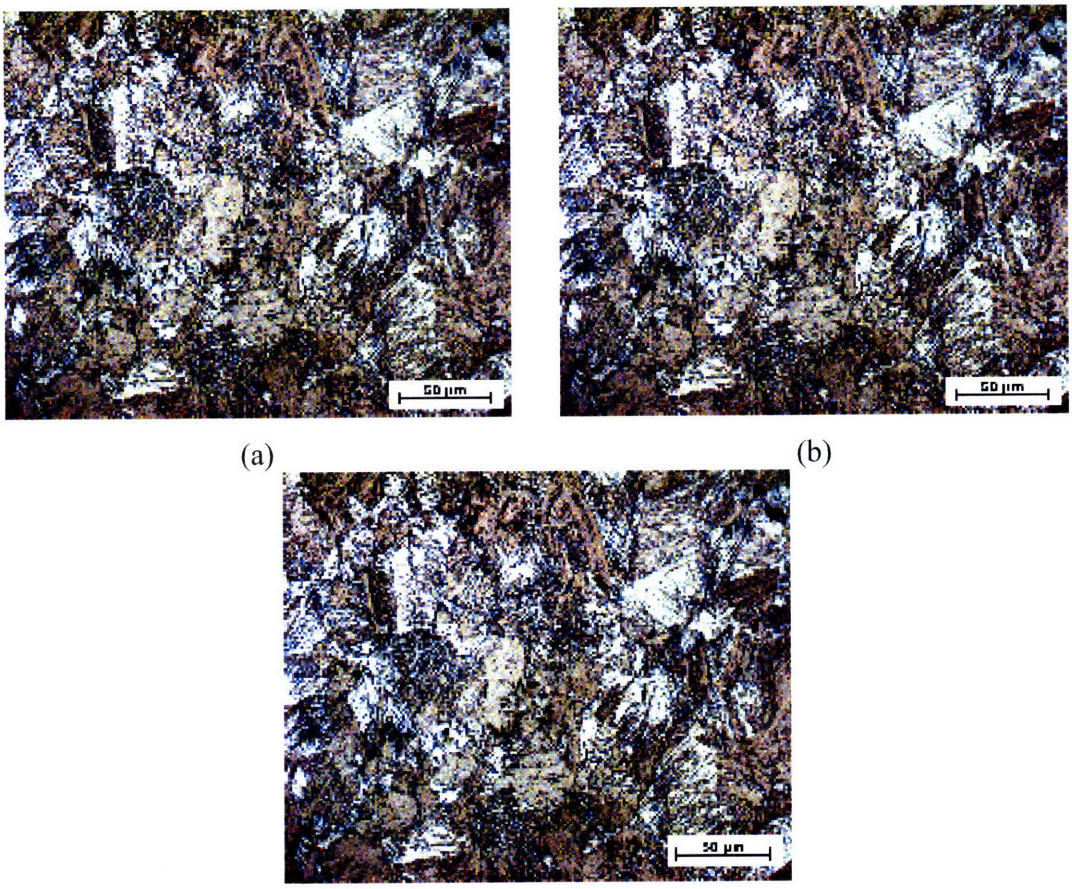

(a) (b)

(c)

Figure 30: Three micrographs of specimen 003-2, which has been strained 10% in the material rolling direction at a magnification of 50x. Each micrograph shows the same image, but the image was taken at a different level of reflected light in the microscope. The percentage of the available reflected light supplied to the microscope used in micrograph (a) is 70%, (b) is 75%, and (c) is 80%.

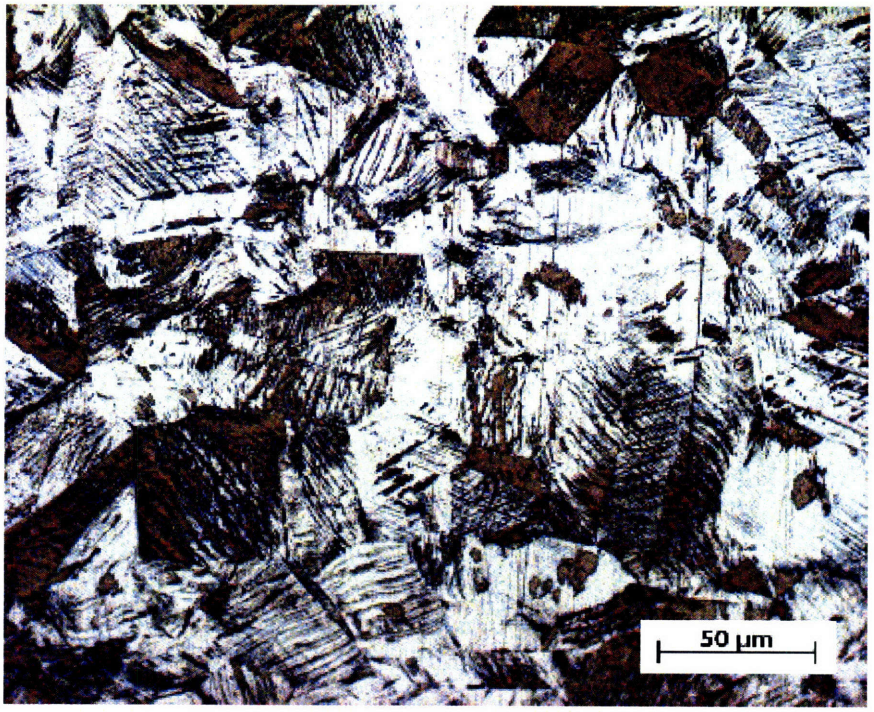

Figure 31: Micrograph of specimens cut from original cold-rolled stainless steel 301LN sheet examined at a magnification of 50x.

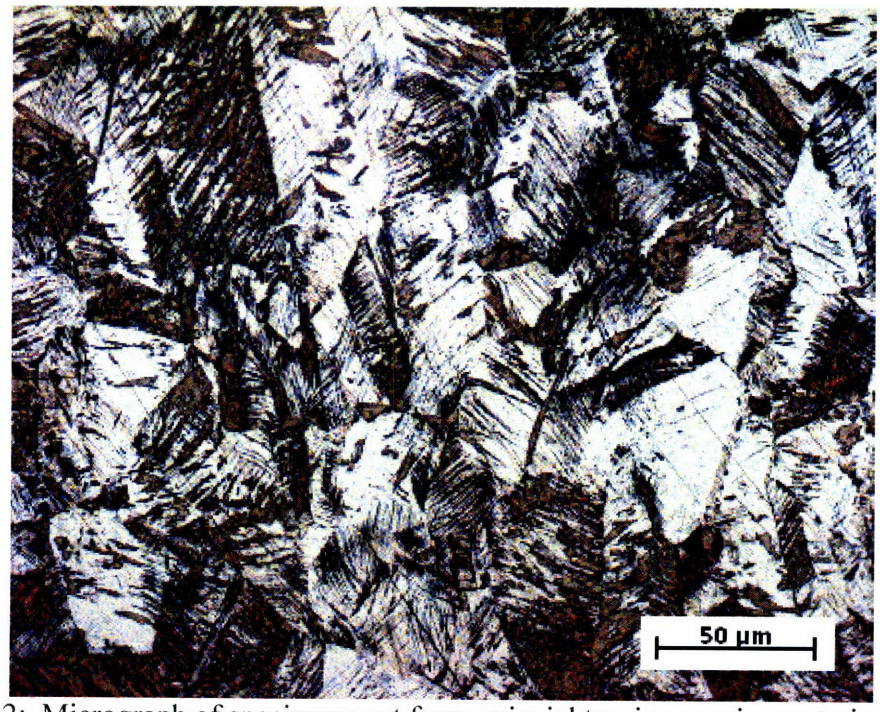

Figure 32: Micrograph of specimens cut from uniaxial tension specimen strained 5% in the material rolling direction examined at a magnification of 50x.

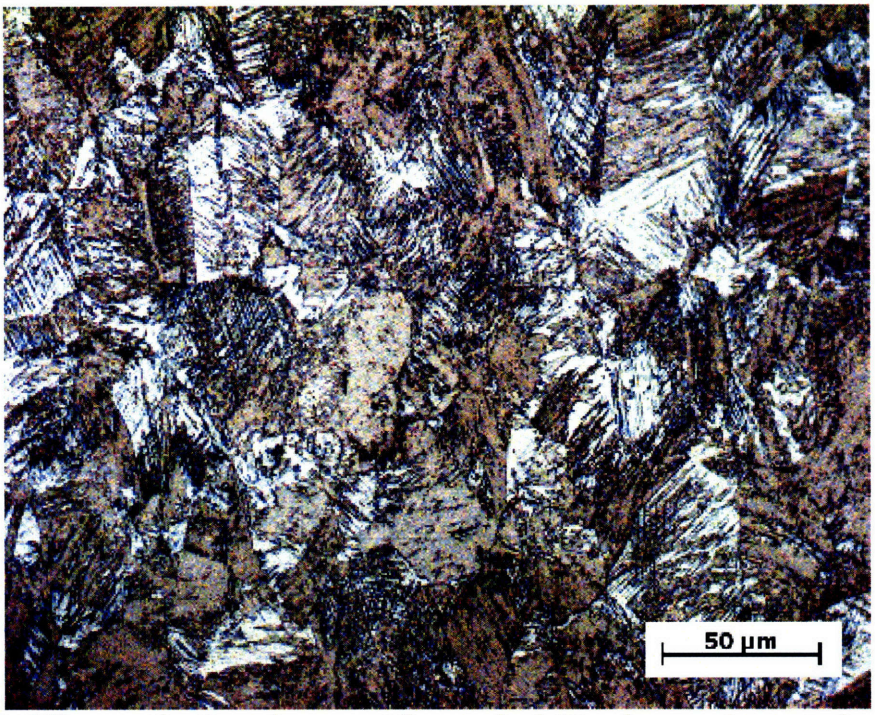

Figure 33: Micrograph of specimens cut from uniaxial tension specimen strained 10% in the material rolling direction examined at a magnification of 50x.

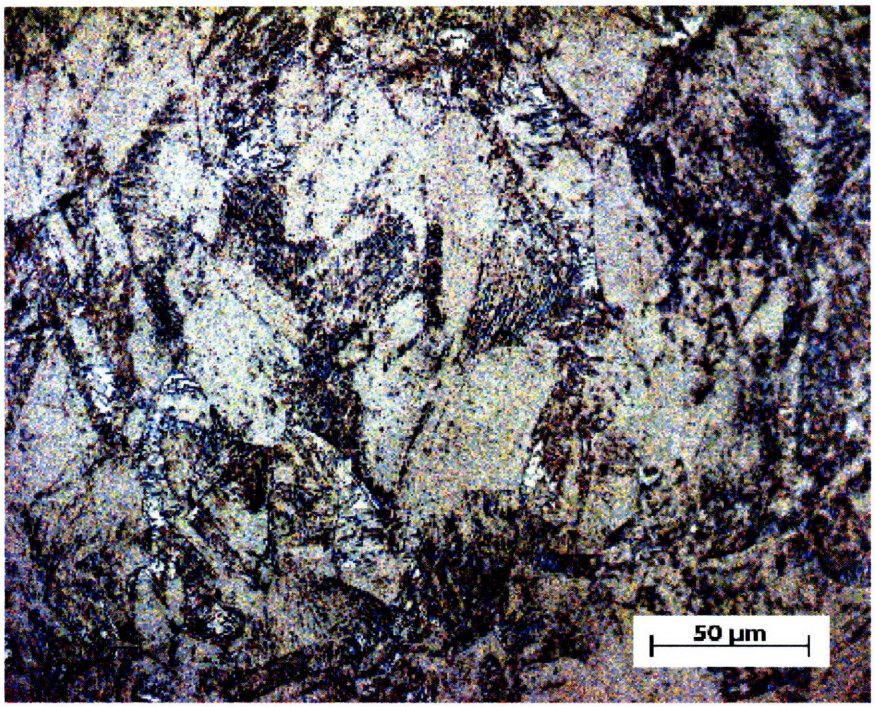

Figure 34: Micrograph of specimens cut from uniaxial tension specimen strained 15% in the material rolling direction examined at a magnification of 50x.

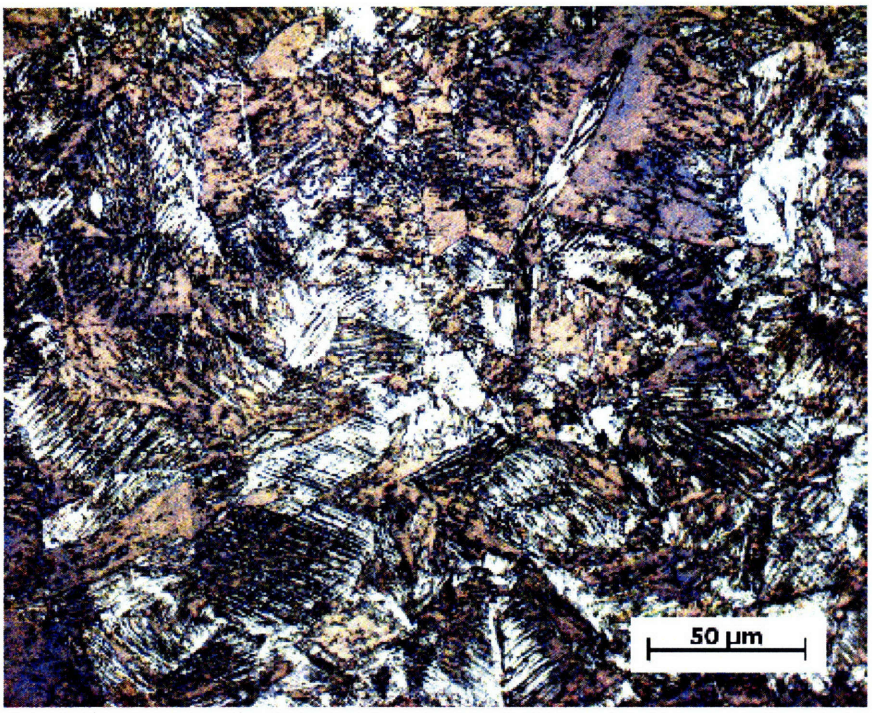

Figure 35: Micrograph of mini-specimen strained 15% in the material cross-rolling direction examined at a magnification of 50x.

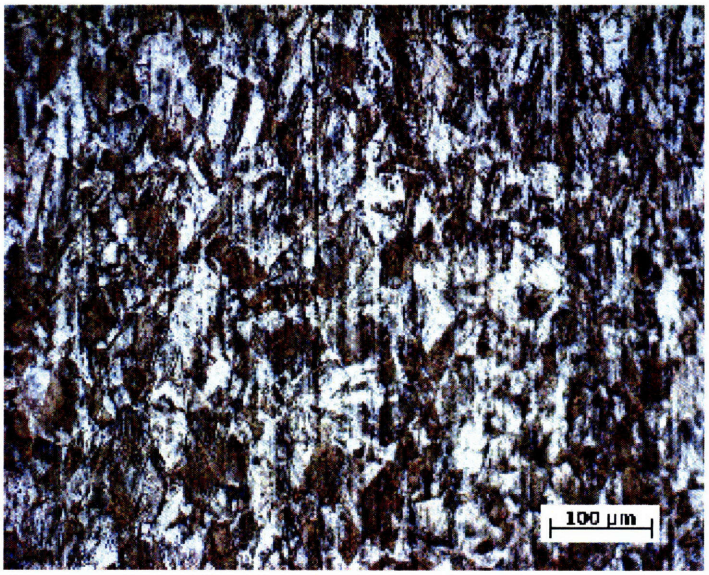

Figure 36: Micrograph of through-thickness gauge section of specimens cut from uniaxial tension specimen strained 5% in the material rolling direction examined at a magnification of 20x. Thickness direction is horizontal.

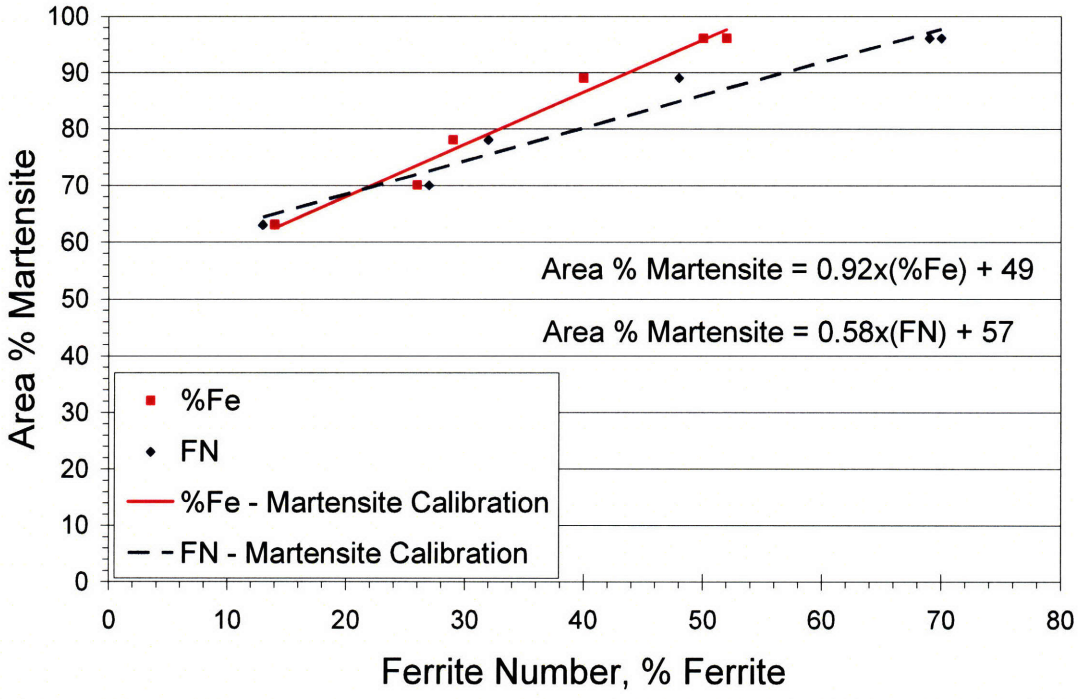

Figure 37: Area percent martensite calculated from micrography versus Ferrite Number and % ferrite output from Feritscope, showing the initial calibration curves between martensite content and FN or percent ferrite.

Table 15: Average area (and assumed volume) percent martensite calculated from micrographs of several stainless steel 301LN specimens.

Specimen	% Strain	Direction of strain	FN	%Fe	Area of Martensite from Micrography	Martensite predicted by FN calibration curve	% Error
original	0	-	13	14	63	64	-2.2
004	5	rolling	27	26	70	73	-3.6
90-15	15	cross	32	29	78	75	3.2
003	10	rolling	48	40	89	85	4.7
001	15	rolling	69	50	96	97	-1.2
002	15	rolling	70	52	96	98	-1.8

The major issue with the current micrographs is that mechanical polishing plastically deforms the polished surface, possibly triggering additional phase transformation on the surface. Thus the martensite on the surface may not be representative of the entire sample volume. In future research for this study, electropolishing will be performed after mechanical polishing in order to remove any surface artifacts from mechanical polishing. Then the specimen will be etched and micrographs will be produced to calibrate the Feritscope accurately.

4.3.3 Conclusions

Micrography is a powerful tool in allowing for the examination of the microstructure. However, micrography requires a very precise procedure and interrupted tests. A qualitative comparison between calculations obtained through microscopy and the use of the Feritscope show good agreement, which indicates that the micrographs can be used to calibrate the Feritscope, and subsequent tests can be performed using the Feritscope to track in-situ martensite evolution.

One of the biggest obstacles in the microscope calculations is in quantifying micrographs is in the image processing of the micrograph, which can result in misinterpretation of the data or loss of information. The major source of error is due to the fact that interpreting the micrographs is somewhat subjective. However, the method of using manual probing of the micrograph to determine the threshold between austenite and martensite eliminates the dependence on etching time and microscope illumination.

Another uncertainty in calculations from micrographs stems from the conversion from area of martensite in one plane to the overall volume content of martensite. In this thesis, the area percentage of martensite was taken to equal the volume percentage of martensite. However, this essentially assumes that the martensite fibers or grains seen in the micrograph simply project through the thickness of the material, and does not account for the three-dimensional shape of martensite. Micrographs of the through-thickness distribution of martensite indicate that martensite is a needle-shaped structure. It is hypothesized that a correction factor will need to be determined to relate area observed in a micrograph to volume of martensite present.

Chapter 5: Comparison of Three Methods of Measuring Martensite

In this thesis, three methods are used for measurement of martensite content in stainless steel 301LN. It is important to note that all three methods of measuring the martensite content in stainless steel 301LN produce the same general trend as well as the same order of magnitude of content of martensite versus plastic strain and material direction at room temperature using quasi-static loading, as demonstrated in Figure 38. All three methods show an increase in martensite content with increasing strain, as was expected. After using the calibration from FN to martensite content, the volume content predicted by each method at different levels of strain can be compared, as shown in Figure 39. This plot shows that at any given finite strain, the martensite content is higher if the material has been stretched along the rolling direction than if it has been stretched along the cross-rolling direction of 45-degrees from the rolling direction. Measurements for martensite in the direction 45-degrees from the rolling direction were only performed using the Feritscope, and this indicated that there is not a significant difference in the martensite developed by uniaxial tension in this direction as compared to the cross-rolling direction.

X-ray diffraction and micrography both require interrupted tests, therefore measurements can only be taken at finite intervals, and both of these processes are very labor intensive. The Feritscope provides an advantage by allowing in-situ measurements, and therefore real-time evolution of the martensite content, but the Feritscope must be calibrated by another measurement method. It is important to address the limitations in each of the measurement techniques.

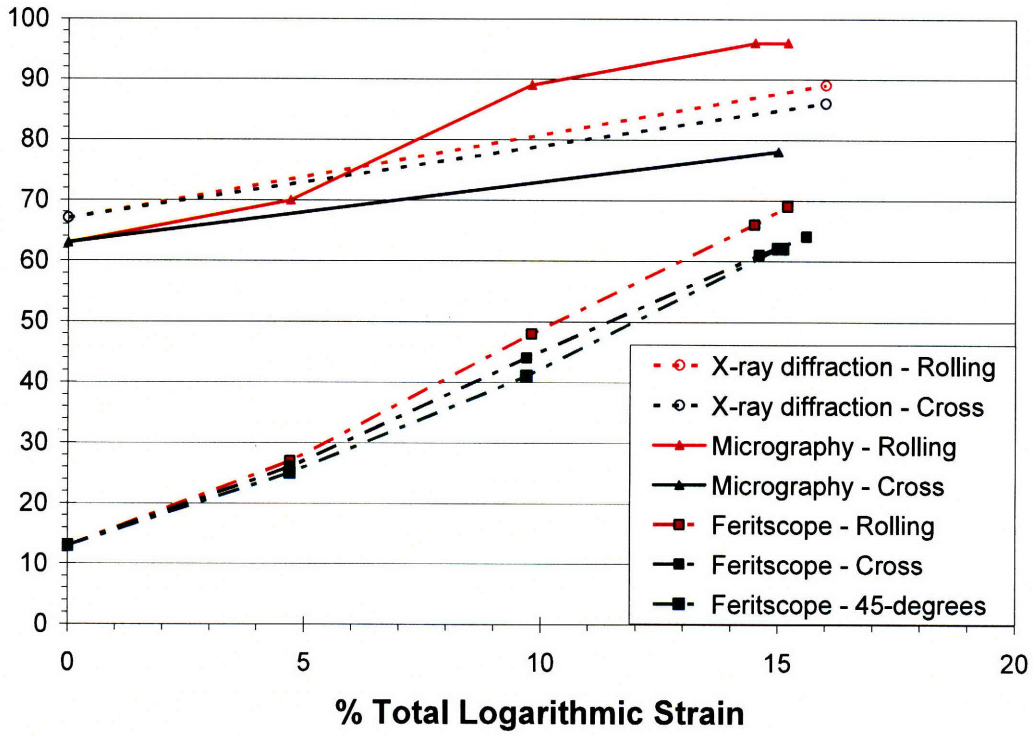

Figure 38: Martensite calculations versus total logarithmic strain. X-ray diffraction and micrography measurements are given in volume percent martensite, while Feritscope measurements are given in FN.

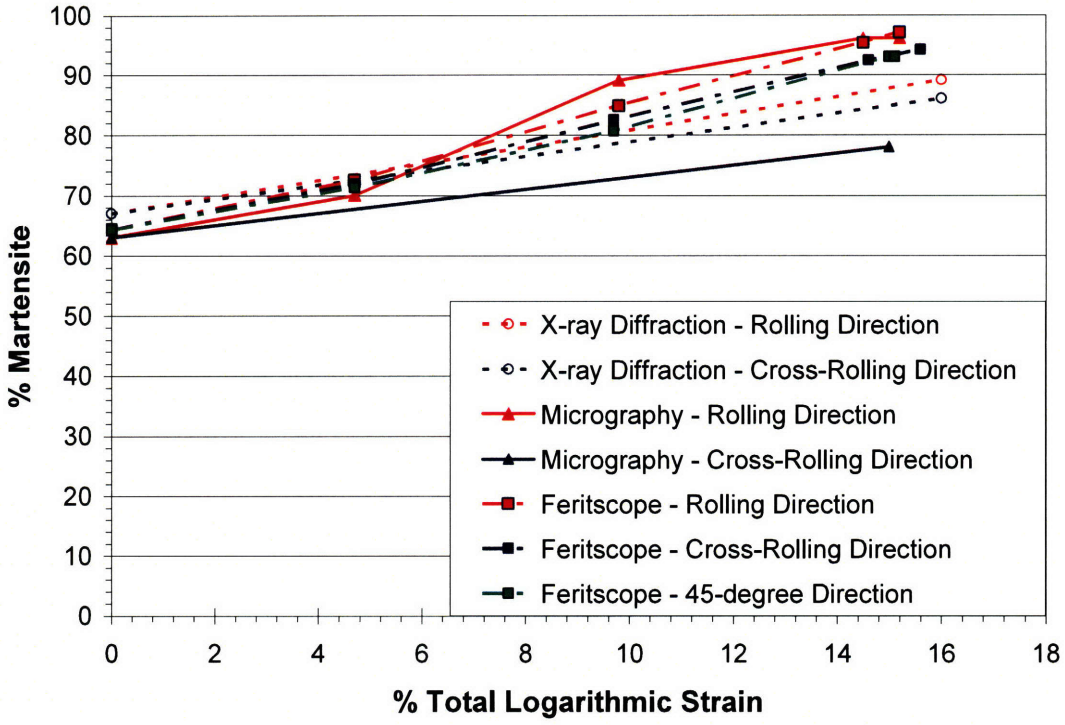

Figure 39: Volume percent martensite predicted using the three measurement methods discussed. Red lines compare results between specimens strained in the rolling direction, blue lines compare results between specimens strained in the cross-rolling direction, and the green line is data from specimens strained at 45-degrees from the rolling direction.

5.1 X-Ray Diffraction

The X-ray diffraction study resulted in the conclusion that the volume of martensite ranged from 67% in the original specimen to 89% in those with about 15% plastic strain. The major source of error present in these measurements is introduced by texture inherent in each of the specimens. If there is significant texture in the specimen being examined, the underlying assumption necessary for accurate X-ray diffraction is violated. This means that, while attempts were made to model the texture, if the volumes analyzed contain significant texture, some attributes would have been exaggerated while others would have been suppressed. Therefore, it cannot be concluded that the resulting volume measurements are absolute.

In addition, for the samples examined, the X-ray penetration depth was calculated to be only about 4 μm to 13 μm, meaning the volume examined was about 0.064 mm^3. The thickness of the specimens ranges from 1.5 *mm* to 1.4 *mm*. Therefore, the maximum depth of penetration of the X-rays is less than 1% of the specimen thickness, and only the material at the surface and slightly below is being studied. This means if there is any gradient in martensite content through the thickness of the specimen, which is possible considering that the cross section area is almost a square (2 *mm* by 1.5 *mm*), the measurements reported may not accurately represent the bulk volume of the specimen.

The final issue with this technique is that in order to analyze the output data, the chemical composition must be provided to the computer software used for the computations. The composition provided was 18% chromium, 7% nickel, and the remainder of the weight percent was given as iron. There are other components in this steel which were not included but which may alter the output of the analysis. Because of the complexity of Jade, and the fact that each additional element has its own suite of refining tools which may be adjusted by the operator, additional sources of error are added with each additional element. Therefore, although adding the other components of the stainless steel would have provided a more precise description of the material and possibly increased the accuracy of the output, it would have also increased the sources for error.

5.2 Micrography

The current method for measuring martensite content from micrographs requires manual probing of the micrograph in order to precisely locate the martensite regions. This could introduce human error into the measurement. However, the predicted areas of martensite from this method are believed to be within +/- 5% of the actual martensite area of the micrograph. By using this method, the ability of the variables of etching procedure and microscope illumination to affect the calculations of martensite is greatly reduced.

Another difficulty is that micrographs produced only indicate the area percentage of martensite in the current plane. Above, efforts were made to determine the through-thickness shape and spatial distribution of martensite. However, each micrograph still only shows data from a single plane. It is believed that with further study of through-

thickness micrographs, a correction factor can be introduced which relates the area of martensite measured in one plane to the overall volume of martensite in the sample. An alternative method for obtaining through-thickness data is to take many micrographs through the thickness of the same specimen to ensure a precise and representative calculation of the martensite content in the entire specimen. This approach is extremely time consuming and may still not capture the three-dimensional shape of the martensite if the thickness removed between subsequent micrographs is more than the size of a grain of martensite.

Finally, as noted above, mechanical polishing may induce martensite at the polished surface of the specimen. Therefore a micrograph produced after etching a mechanically polished specimen is expected to result in an overestimate of volumetric martensite content because the surface concentration is higher than the bulk of the material. Electropolishing should be used to remove all of this martensite which was induced during grinding and polishing, and not representative of the strained test specimen's bulk gauge section volume. This additional step has not yet been carried out.

5.3 Magnetic Induction Method Employing Feritscope

The Feritscope relies on another method of measurement for accurate calibration. In this case, micrography is recommended. However, this requires interrupted tests, and only one strain level and FN number can be analyzed per specimen. If the FN curve is not directly proportional to martensite content, the finite number of micrographs may not adequately capture the nonlinearity. However, it is believed that this method is the most powerful and can be adequately calibrated.

5.4 Error Analysis

There are several sources of error in each of the three measurement methods used. Error estimations are described for each of the methods here. Mohr and Jacquemin (2008) state that the martensite content in the original cold-rolled Arcelor-Mittal stainless steel 301LN sheet material is 24%. In order to have a baseline with which to calculate errors, the reference value of 24% martensite in the original material is used, and each

measurement method will be compared with this reference volume percentage of martensite.

The main sources of error present in X-ray diffraction analysis are texture of the specimens and the shallow penetration depth of the X-ray. Although the texture effect cannot be ignored, the texture was modeled using software to remove its affect on the results, leading to a prediction within +/-2% using the given data. Therefore, the remaining prominent source of error is due to the shallow depth of X-ray penetration, which has two manifestations. First, the surfaces of the specimens were cleaned with acetone before the X-ray diffraction studies; however, it is likely that there were substances on the surface of the specimens which could affect the measurements by either introducing other elements, or decreasing the effective depth of examination. Second, the cross sections of the specimens did not provide for a uniform stress or strain state through the thickness, therefore the gradient of stress and strain would likely cause a gradient of martensite evolution. Therefore, the martensite content at the surface of the specimen may exceed that in the center of the specimen. Through X-ray diffraction, the original specimen was measured to have about 67% volume percent martensite. When comparing this value with that of the reference value, X-ray diffraction overestimates the volume percentage by about 40%, which corresponds to an 80% overestimate of the martensite content. An error band of fixed value of 40% is applied to each measured value from X-ray diffraction. A corrected X-ray diffraction prediction including uncertainty in the X-ray diffraction study versus logarithmic strain is given in Figure 40. This error could be decreased by electropolishing the surface of the specimen to remove any surface contamination. In addition, a specimen with a uniform strain field should be used to eliminate the large gradients in strain expected in the current samples. In this case, electropolishing is also recommended in order to examine a plane closer to the center of the specimen, and not one on the surface which has a different state of stress than the very center of the specimen. The error in the results after modeling the texture were determined to be within +/-2%, so with electropolishing, the error should be about +/-2%.

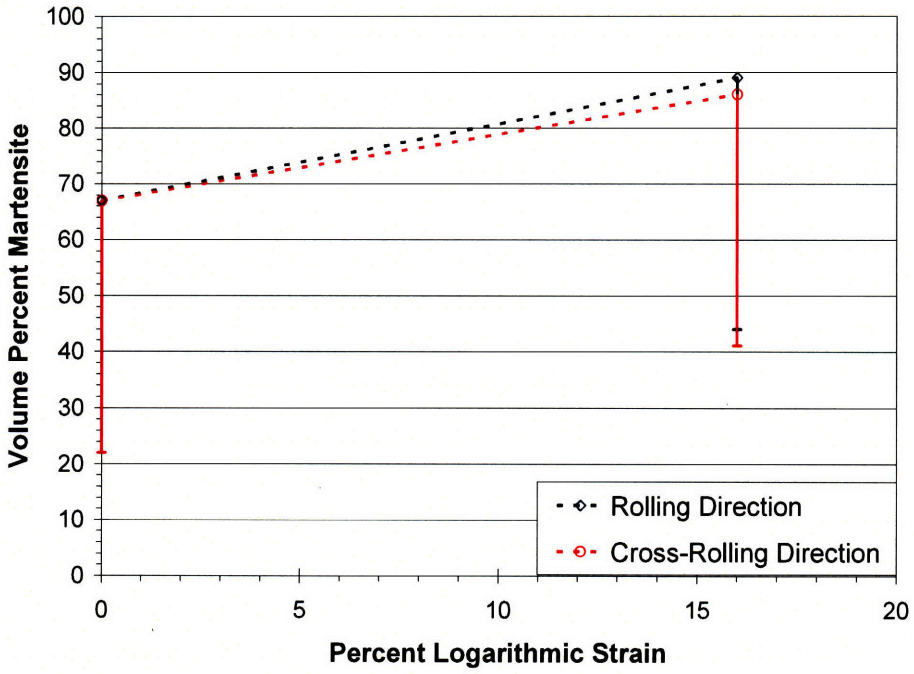

Figure 40: Percent martensite versus percent logarithmic strain from X-ray diffraction analysis including expected error.

As stated in the Fischer operating manual for the Feritscope MP30E, the error in converting FN to percent ferrite is about 15%. Therefore, a similar error is assumed for converting between FN and percent martensite. This error is incorporated into the calibration curve and is shown in

Figure 41 Because this error is inherent in the Feritscope, it is difficult to resolve. Therefore, it is believed that the size of this error band cannot be mediated and will remain at +/- 15%.

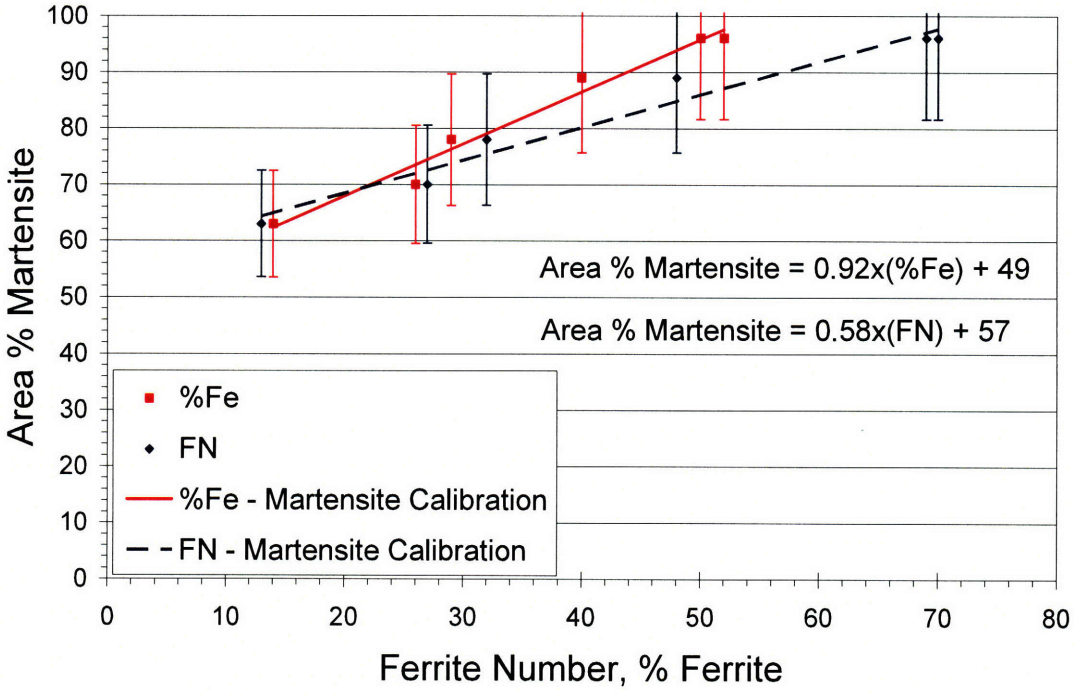

Figure 41: Calibration between area percent martensite and Ferrite Number or percent ferrite including expected calibration error of 15%.

The sources of error in micrography can be separated into two sources. The first source of error is in the analysis of the resulting micrographs. The threshold between martensite and austenite is adjusted for each micrograph after careful probing of the range of intensity values for each phase in the micrograph. From several iterations of this process, it was determined that the threshold can be reasonably determined in an intensity range of +/- 5. Changing the threshold by this intensity results in a typical variation in the martensite percentage of +/-5%, and a maximum variation of calculated martensite percentage of +/- 10%. Therefore, the error of +/- 10% is expected in the measurements. In order to mediate this error, more filters could be applied to the micrographs to increase the contrast. However, this may result in loss of information. It is noted that some of the micrographs, while having a very sharp image in the center, had blurry edges. This inevitably leads to miscalculation of error. This blurriness could be decreased by using different lenses in the microscope, or by only using the clear part of the micrograph for

data analysis. Therefore, more research is required to determine how to decrease the error in analyzing the micrographs. The second source of error in measurements from the present micrographs is from the induced martensite at the surface due to mechanical polishing. This means that the martensite viewed in the micrographs is higher than is representative of the volume. Comparing the base sheet metal reference value of 24% martensite to the micrograph prediction of 63% martensite, the current micrograph measurements overestimate the martensite content by about 40%, or with an error of about 60%. Figure 42 shows the plot of martensite content versus percent strain after applying an error band demonstrating a constant overestimation of 40%. It is believed that after electropolishing is performed, this error will be eliminated as well as possible. Therefore, the micrograph should indicate the martensite content of the bulk of the sample, essentially eliminating this error.

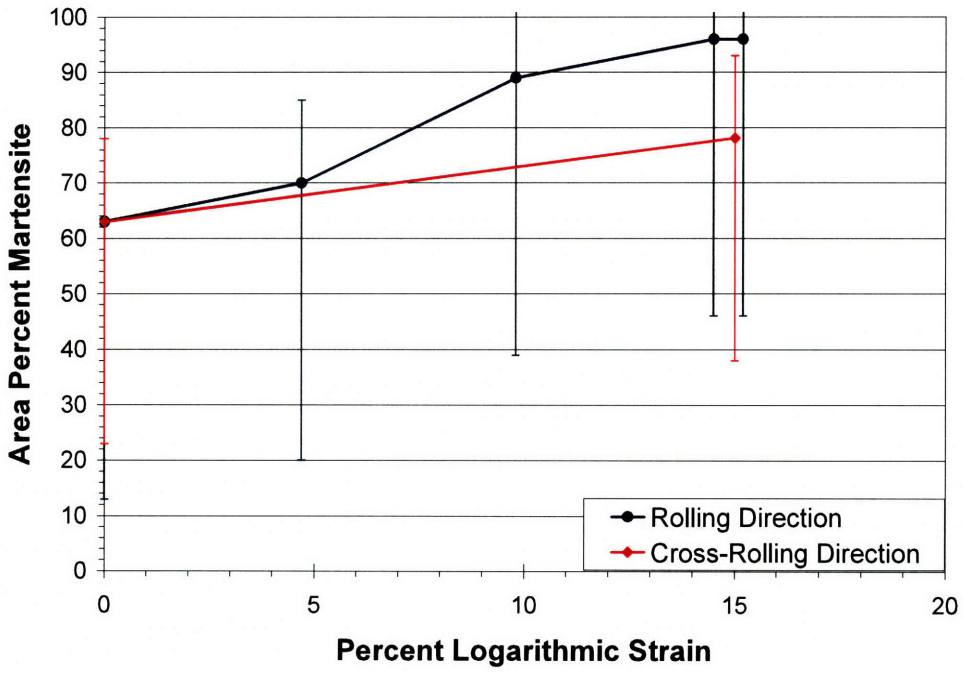

Figure 42: Percent martensite versus percent logarithmic strain from microscopy measurements including expected error from measuring technique and from martensite formed during mechanical polishing.

In conclusion, each of the measurements has an inherent amount of error, but it is believed that some of these errors can be reduced with further modifications of the measurement techniques. In particular, the errors due to the shallow penetration depth during X-ray diffraction should be essentially eliminated by electropolishing the gauge section of more suitably designed specimens with minimal stress or strain gradients. In addition, electropolishing of the polished specimens should dramatically decrease the error in micrograph analysis by removing martensite induced on the surface from mechanical polishing in order to provide a more representative martensite content of the volume. The 15% measurement error in the Feritscope calibration cannot be eliminated, and must always be taken into account. In addition, reducing the error due to analysis of the micrographs via adjusting the threshold for differentiation between austenite and martensite requires more investigation. The plot in Figure 43 shows the current errors present in the analysis, and an updated plot of the martensite content versus logarithmic strain is given in Figure 44, which shows the expected improvement in measurements with adjustments above included. This shows that the measurements do overlap, and while the repeatability of the Feritscope measurements during in-situ tests does still indicate a reasonable directional dependence on the martensite evolution, accounting for the uncertainties and possible errors leads to a decreased directional dependence.

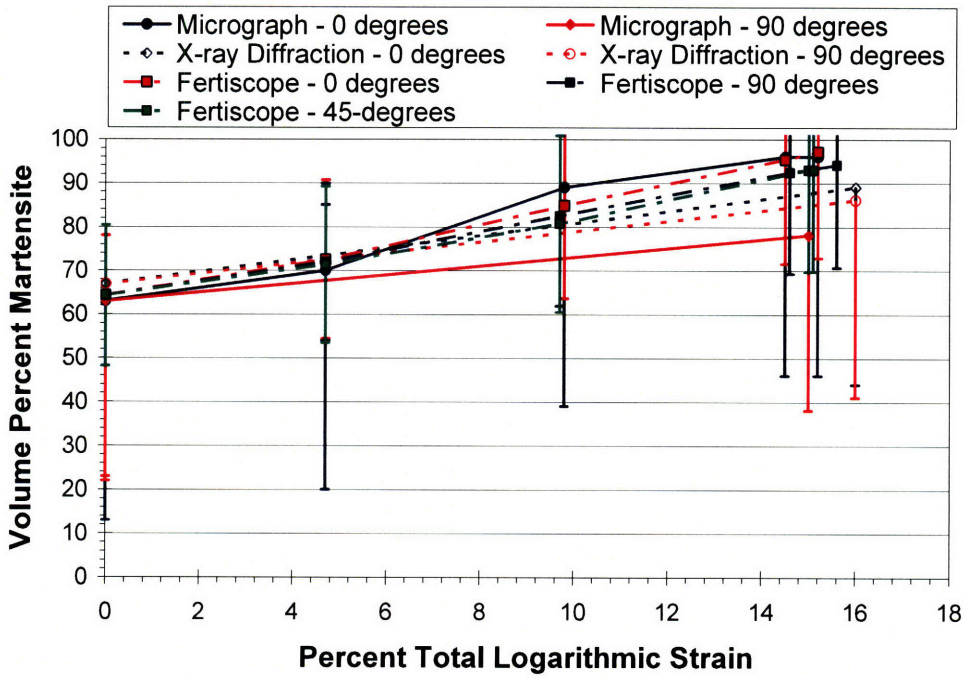

Figure 43: Percent martensite versus percent logarithmic strain for three methods of measurement including current maximum error.

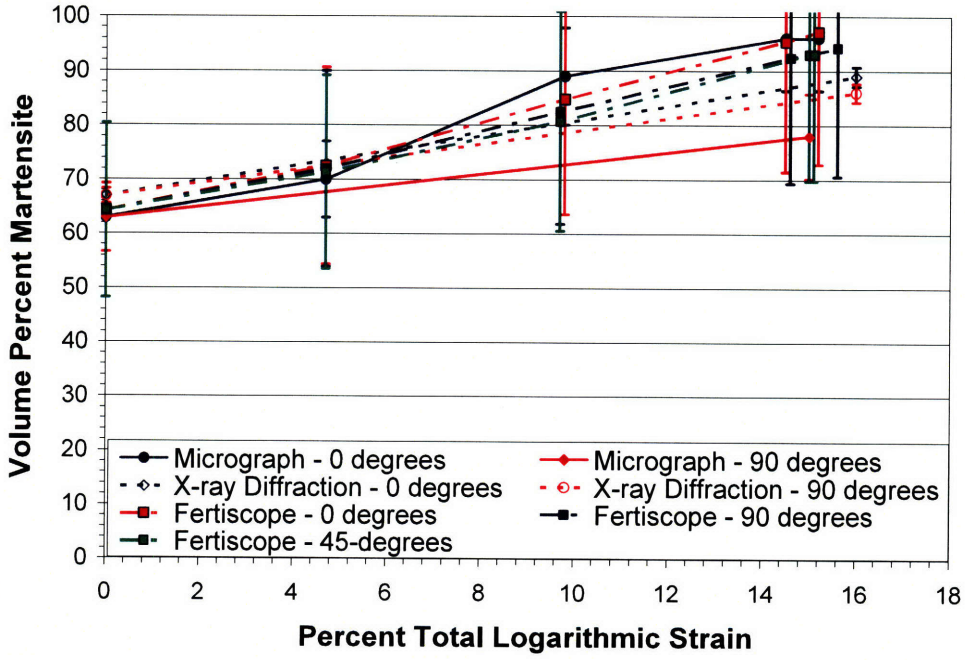

Figure 44: Percent martensite versus percent logarithmic strain from microscopy measurements including projected maximum error after adjustments to procedures.

Chapter 6: Conclusions

In studying the plastic behavior of austenitic stainless steel, it is imperative to recognize the inherent anisotropy in the cold-rolled sheets as well as the importance of the microscopic phase transformation from austenite to martensite. This thesis details testing procedures used to determine the anisotropy present in the sheets from cold-rolling. The effect of plastic strain in one direction on the subsequent flow strength in a different material direction is studied with respect to initial anisotropy as well as the microscopic phase transformation.

The initial anisotropy in the material is due to the cold-rolling processing to create sheets of stainless steel. This discrepancy in material properties in different directions is enhanced when the material is subjected to complicated loading history by being strained in the rolling direction and subsequently in the cross-rolling direction. The cross-hardening study reveals that straining the material in the rolling direction and subsequently in the cross-rolling direction results in increased flow strength in the cross-rolling direction as compared with the flow strength in a specimen at the same equivalent plastic strain that has only been loaded in the cross direction. The opposite is true when the specimen is first subjected to loading in the cross-rolling direction and then in the rolling direction – the subsequent flow strength is lower in the material once it has been pre-strained in the cross direction than had it only been strained in the rolling direction. This indicates that the microstructural evolution that dictates the macroscopic behavior is different depending on the material direction, leading to disparate hardening curves.

This research has revealed that there is indeed a directional dependence on the martensitic evolution during strain-induced phase transformation. More martensite is produced when applying tension in the material rolling direction than in the material cross-rolling direction. The amount martensite produced in the direction 45 degrees from the rolling direction is in between the amount produced in the rolling and cross-rolling directions. Once some of the austenite has been transformed into martensite, the material can be viewed as a two-phase composite structure with brittle martensite and ductile austenite. Because martensite is stronger and harder than austenite, the introduction of

martensite affects the strain-hardening behavior of stainless steel 301LN, and possibly its fracture properties.

Three techniques for quantifying the martensite content are executed and evaluated. X-ray diffraction and microscopy both require interrupted tests, while the use of the Feritscope allows for in-situ measurement of martensite content. All three methods of measurement result in different scales for martensite measurement, and proper calibration of the Feritscope must be performed by comparison with micrographs for absolute quantitative analysis. The qualitative trends of martensite evolution are consistent in X-ray diffraction and the use of the Feritscope, with much scatter present in the microscopy method of measurement. The martensite content is highest in specimens strained in the rolling direction, followed by specimens strained in the cross-rolling direction, and lowest in the specimens extracted from the as-received cold-rolled sheets. The martensite content in the 45-degree specimen was only measured using the Feritscope and results indicated that its martensite content falls between that of the specimens strained in the rolling and cross-rolling directions.

An initial calibration of the Feritscope was performed using area measurements from micrographs. Additional micrographs will be used to obtain more data points in the calibration curve between martensite content and FN. It is believed that the current calibration of the Feritscope over predicts the martensite content because of the additional martensite present at the surface of the specimens due to plastic deformation during polishing processes. This additional martensite will be removed via electropolishing, and a more accurate calibration should be obtained. However, as mentioned previously, the uncertainties and inherent errors in each of the methods still results in a large amount of error. Therefore, although it is deemed that there is a directional dependence on martensite evolution, including the possible errors causes the curves in the three material directions studied to overlap. Accounting for the errors eradicates any significant directional dependence on martensite evolution.

Chapter 7: Future Work

For accurate quantitative results, full calibration of the Feritscope must be performed. This will require electropolishing the mechanically polished specimens to dissolve any martensite induced on the surface of the sample. Then the specimens will be etched and micrographs will be made. The area percentage of martensite viewed in the micrograph will then be related to the FN reading from the Feritscope. Calibration of the Feritscope will allow for a conversion between FN and volume percent martensite which can then be used in subsequent analysis to allow continuous monitoring of the martensite volume during various tests.

In addition, the dependence of martensite evolution on stress state will be examined by subjecting specimens to various combinations of shear and tensile or compressive loading. Testing in a controlled temperature environment will reveal the effect of temperature on the martensite content. This information will be useful because in crash situations, the impact creates an essentially adiabatic loading of the material, hence a sharp increase in temperature. Therefore, by testing the material at various temperatures, some insight into possible rate-dependence of the martensite evolution can be gained.

The martensite transformation kinetics law will then be constructed to include the effects of anisotropy (or material direction), stress state, and temperature on the martensite evolution and the subsequent flow stress of the material. Validation tests will be performed, and the constitutive model will be evaluated through numerical analysis to determine if it has adequate predictive capabilities.

References

Abaqus, Abaqus documentation, version 6.5-1, 2006.

American Society for Metals, Metals Handbook: Metallography, Structures and Phase Diagrams, 8th Edition, Vol. 8, Metals Park, Ohio: American Society for Metals, 1973.

ASTM Standard E975-03, Standard Practice for X-Ray Determination of Retained Austenite in Steel with Near Random Crystallographic Orientation, 2003.

Barlat F, Lian J, Plastic behavior and stretchability of sheet metals. Part I: A yield function for orthotropic sheets under plane stress conditions, Int. J. Plasticity 5. pp. 51-66, 1989.

Barlat F, Lege D, and Brem J, A six-component yield function for anisotropic materials. International Journal of Plasticity, 7, pp 693-712, 1991.

Budinski, Kenneth G, and Michael K Budinski, Engineering Materials Properties and Selections, Prentice-Hall, Inc. 1999.

De, Amar K, John G Speer, David K Matlock, David C Murdock, Martin C Mataya, and Robert J Comstock, Jr., Deformation-Induced Phase Transformation and Strain Hardening in Type 304 Austenitic Stainless Steel, Metallurgical and Materials Transactions A, Volume 37, Number 6, pp. 1875-1886, June 2006.

Diani JM, and Parks DM. Effects of strain state on the kinetics of strain-induced martensite in steels, J. Mech. Phys. Solids, Volume 49, Number 9, pp. 1613-1635, 1998.

Hill R, A theory of the yielding and plastic flow of anisotropic metals, Proc. Royal Soc. London A193, pp. 281-297, 1948.

Hill R, Constitutive modeling of orthotropic plasticity in sheet metals, J. Mech. Phys. Solids 38(3), pp. 405-417, 1990.

ISO 8249: Welding – Determination of Ferrite Number (FN) in austenitic and duplex ferritic austenitic Cr-Ni stainless steel weld metals, 2000.

Jenkins R, and Snyder R, Introduction to X-ray Powder Diffractometry, Wiley-Interscience, 1996.

Karafillis AP, Boyce MC, A general anisotropic yield criterion using bounds and a transformation weighting tensor, J. Mech. Phys. Solids 41(12), pp. 1859-1886, 1993.

Mohr D, Jacquemin J, Large deformation of anisotropic austenitic stainless steel sheets at room temperature: multi-axial experiments and phenomenological modeling, Submitted for publication, 2008.

Olsen GB, Cohen M, Kinetics of strain-induced martensitic nucleation, Metallurgical Transactions 6A, pp. 791-795, 1975.

Olsen GB, Cohen M, Stress-assisted isothermal martensitic transformation: application to TRIP steels, Metallurgical Transactions 13A, pp/ 1907-1914, 1982.

Plunkett B, Lebenson R, Cazacu O, & Barlat F, Anisotropic Yield Function of Hexagonal Materials Taking into Account Texture Development and Anisotropic Hardening. Acta Materiala , 54 (16), 2006.

Stringfellow RG, Parks DM, Olsen GB, A constitutive model for transformation plasticity accompanying strain-induced martensitic transformations in metastable austenitic steels, Acta Metall. Mater. 40(7), pp. 1703-1716, 1992.

Appendix A: Equivalent plastic strain definition

The equivalent plastic strain rate is defined as the work-conjugate strain measure to the equivalent stress. In the general three-dimensional case the incremental plastic dissipation, $d\psi$, is given by the inner product of the Cauchy stress tensor, $\boldsymbol{\sigma}$, and the plastic strain increment tensor, $d\boldsymbol{\varepsilon}^p$.

$$d\psi = \boldsymbol{\sigma} : d\boldsymbol{\varepsilon}^p = \sigma_{ij}(d\varepsilon_{ij}^p) = \sigma_{11}(d\varepsilon_{11}^p) + \sigma_{12}(d\varepsilon_{12}^p) + \ldots + \sigma_{33}(d\varepsilon_{33}^p) \tag{1}$$

The plastic strain increment tensor is constitutively prescribed by the flow rule. In the case of an associated flow rule, it reads:

$$d\boldsymbol{\varepsilon}^p = \frac{\partial f}{\partial \boldsymbol{\sigma}}(d\gamma), \tag{2}$$

where the function $f = f(\boldsymbol{\sigma})$ defines the yield surface, and $d\gamma$ is the plastic multiplier.

Many yield functions are written in the form:

$$f(\boldsymbol{\sigma}) = \bar{\sigma} - k, \tag{3}$$

where the equivalent stress, $\bar{\sigma} = \bar{\sigma}(\boldsymbol{\sigma})$, is defined such that it is equal to the applied stress in a uniaxial tensile or compression test. The scalar k quantifies the deformation resistance of the material. Based on this definition, k is the flow stress under uniaxial conditions.

Several researchers define the equivalent stress as a homogeneous function of degree n of the stress tensor. Thus, according to Euler's theorem, the following identity holds true:

$$n\bar{\sigma} = \frac{\partial \bar{\sigma}}{\partial \boldsymbol{\sigma}} : \boldsymbol{\sigma} = \frac{\partial \bar{\sigma}}{\partial \sigma_{ij}} : \sigma_{ij} \tag{4}$$

Combining Eqns. (1) through (4) gives the following definition for the plastic dissipation:

$$d\psi = \boldsymbol{\sigma} : d\boldsymbol{\varepsilon}^p = \boldsymbol{\sigma} : \frac{\partial f}{\partial \boldsymbol{\sigma}}(d\gamma) = \left[\boldsymbol{\sigma} : \frac{\partial \bar{\sigma}}{\partial \boldsymbol{\sigma}}\right](d\gamma) = n\bar{\sigma}(d\gamma) \tag{5}$$

Eqn. (5) demonstrates that there exists a work-conjugate strain increment, $d\bar{\varepsilon}^p$, to the equivalent stress,

$$d\bar{\varepsilon}^p = n(d\gamma) \tag{6}$$

such that the plastic dissipation may be calculated from the product of these two scalar measures of stress and deformation,

$$\boldsymbol{\sigma} : d\boldsymbol{\varepsilon}^p = \bar{\sigma}(d\bar{\varepsilon}^p) \tag{7}$$

The integral of this plastic strain increment, $d\bar{\varepsilon}^p$, is referred to as the total equivalent plastic strain:

$$\bar{\varepsilon}^p(t) = \int d\bar{\varepsilon}^p = \int_0^t \dot{\bar{\varepsilon}}^p dt \tag{8}$$

where it is assumed that $\bar{\varepsilon}^p = 0$ before applying a deformation history over the time t.

The explicit mathematical expression for the equivalent plastic strain depends on the definition of the equivalent stress. Therefore, when referring to the equivalent plastic strain, the yield function must be specified. Once the type of yield criterion is specified (e.g., von Mises, Hill 1948, etc.), the equivalent plastic strain may be determined from Eqn. (7).

Some definitions of the equivalent stress may be written in the form:

$$\bar{\sigma} = \sqrt{(\mathbf{P}\boldsymbol{\sigma}^v)\cdot\boldsymbol{\sigma}^v} \tag{9}$$

where $\mathbf{P}$ is a symmetric positive-definite matrix and $\boldsymbol{\sigma}^v$ denotes the stress vector (employing Voight notation). Limiting the discussion to plane stress states,

$$\boldsymbol{\sigma}^v = [\sigma_{11} \quad \sigma_{22} \quad \sigma_{12}]^T \tag{10}$$

In this particular case, $\bar{\sigma}$ is a homogeneous function of degree $n = 1$ of the stress vector.

Analogously to Eqn. (10), vector notation for the plastic strain increments gives:

$$d\boldsymbol{\varepsilon}_p^v = [d\varepsilon_{11}^p \quad d\varepsilon_{22}^p \quad 2d\varepsilon_{12}^p]^T \tag{11}$$

Upon evaluation of the flow rule, we find

$$d\boldsymbol{\varepsilon}_p^v = \frac{\partial f}{\partial \boldsymbol{\sigma}^v}(d\gamma) = \frac{\partial f}{\partial \boldsymbol{\sigma}^v}(d\bar{\varepsilon}^p) = \frac{\mathbf{P}\boldsymbol{\sigma}^v}{\bar{\sigma}}(d\bar{\varepsilon}^p) \tag{12}$$

and thus

$$\boldsymbol{\sigma}^{v} = \frac{\bar{\sigma}}{d\bar{\varepsilon}^{p}}\left[\mathbf{P}^{-1}(d\boldsymbol{\varepsilon}_{p}^{v})\right] \tag{13}$$

Using Eqn. (13) for the stress vector in Eqn. (9) yields an explicit expression for the equivalent plastic strain increment:

$$d\bar{\varepsilon}^{p} = \sqrt{[\mathbf{P}^{-1}(d\boldsymbol{\varepsilon}_{p}^{v})]\cdot(d\boldsymbol{\varepsilon}_{p}^{v})} \tag{14}$$

Two examples for derivation of the equivalent plastic strain based on two yield criteria are given below.

Example 1: Von Mises yield function

The equivalent stress of the von Mises yield criterion reads

$$\bar{\sigma} = \sqrt{\sigma_{11}^{2} - \sigma_{11}\sigma_{22} + \sigma_{22}^{2} + 3\sigma_{12}^{2}}$$

which corresponds to

$$\mathbf{P} = \begin{bmatrix} 1 & -1/2 & 0 \\ -1/2 & 1 & 0 \\ 0 & 0 & 3 \end{bmatrix}$$

With the general expression for the equivalent plastic strain increment given in Eqn. 14, the inverse of P is needed. It is given by:

$$\mathbf{P}^{-1} = \begin{bmatrix} 4/3 & 2/3 & 0 \\ 2/3 & 4/3 & 0 \\ 0 & 0 & 1/3 \end{bmatrix}$$

Thus, the explicit mathematical expression of the equivalent plastic strain increment for the von Mises yield criterion is:

$$d\bar{\varepsilon}^{p} = \sqrt{\frac{4}{3}\left[\left(d\varepsilon_{11}^{p}\right)^{2} + \left(d\varepsilon_{22}^{p}\right)^{2} + \left(d\varepsilon_{11}^{p}\right)\cdot\left(d\varepsilon_{22}^{p}\right)\right] + \frac{1}{3}\left(2d\varepsilon_{12}^{p}\right)^{2}}$$

Using the assumption of plastic incompressibility,

$$d\varepsilon_{33}^{p} = -d\varepsilon_{11}^{p} - d\varepsilon_{22}^{p}$$

The expression for equivalent plastic strain increment then becomes:

$$d\bar{\varepsilon}^{p} = \sqrt{\frac{2}{3}\left[\left(d\varepsilon_{11}^{p}\right)^2 + \left(d\varepsilon_{22}^{p}\right)^2 + \left(d\varepsilon_{33}^{p}\right)^2\right] + \frac{4}{3}\left(d\varepsilon_{12}^{p}\right)^2}$$

With shear stresses equal to zero, the expression for equivalent plastic strain increment becomes:

$$d\bar{\varepsilon}^{p} = \sqrt{\frac{2}{3}\left[\left(d\varepsilon_{11}^{p}\right)^2 + \left(d\varepsilon_{22}^{p}\right)^2 + \left(d\varepsilon_{33}^{p}\right)^2\right]}$$

Example 2: Hill 1948 yield function

The equivalent stress of the Hill 1948 yield criterion is given by

$$\bar{\sigma} = \sqrt{(G+H)\sigma_{11}^2 - 2H\sigma_{11}\sigma_{22} + (F+H)\sigma_{22}^2 + 2N\sigma_{12}^2}$$

which corresponds to:

$$\mathbf{P} = \begin{bmatrix} G+H & -H & 0 \\ -H & F+H & 0 \\ 0 & 0 & 2N \end{bmatrix}$$

Note: The stresses and strains are given in defined directions of anisotropy, e.g., σ_{11} is the stress in the material rolling direction, and σ_{22} is the stress in the material cross-rolling direction.

With the general expression for the equivalent plastic strain increment given in Eqn. 11, the inverse of P is needed and is given by:

$$\mathbf{P}^{-1} = \begin{bmatrix} F + H/\alpha & H/\alpha & 0 \\ H/\alpha & G + H/\alpha & 0 \\ 0 & 0 & 1/2N \end{bmatrix}, \qquad \text{where } \alpha = F \cdot G + G \cdot H + H \cdot F$$

Thus, the explicit mathematical expression of the equivalent plastic strain increment for the Hill 1948 yield criterion is:

$$d\varepsilon^p = \sqrt{\frac{1}{\alpha}\left[(F+H)\cdot\left(d\varepsilon_{11}^p\right)^2 + (H+G)\cdot\left(d\varepsilon_{22}^p\right)^2 + (2H)\cdot\left(d\varepsilon_{11}^p\right)\cdot\left(d\varepsilon_{22}^p\right)\right] + \frac{1}{2N}\left(2d\varepsilon_{12}^p\right)^2}$$

Again employing the assumption of plastic incompressibility, the expression for equivalent plastic strain increment becomes:

$$d\varepsilon^p = \sqrt{\frac{1}{\alpha}\left[F\cdot\left(d\varepsilon_{11}^p\right)^2 + G\cdot\left(d\varepsilon_{22}^p\right)^2 + H\cdot\left(d\varepsilon_{33}^p\right)^2\right] + \frac{2}{N}\left(d\varepsilon_{12}^p\right)^2}$$

With shear stresses equal to zero, the expression for equivalent plastic strain increment becomes:

$$d\varepsilon^p = \sqrt{\frac{1}{\alpha}\left[F\cdot\left(d\varepsilon_{11}^p\right)^2 + G\cdot\left(d\varepsilon_{22}^p\right)^2 + H\cdot\left(d\varepsilon_{33}^p\right)^2\right]}$$